Accepted by *Geochemistry, Geophysics, Geosystems*

Source complexity of the 2015 Mw 7.9 Bonin earthquake

Yu Chen[1,2,a,b], Lingsen Meng[3,a], Ailin Zhang[3], Lianxing Wen[1,4]

[1] Stony Brook University, Stony Brook, NY, 11794

[2] Los Alamos National Laboratory, Los Alamos, NM, 87545

[3] University of California, Los Angeles, CA, 90095

[4] Laboratory of Seismology and Physics of Earth's Interior; School of Earth and Space Sciences, University of Science and Technology of China, Hefei, Anhui, 230026

[a] Y.C. and L.M. equally contribute to this paper

[b] Corresponding author: Yu Chen (esschenyu@gmail.com)

Key Points:

- Integrated study using a novel 3D back-projection and multiple-source inversion.
- Non-planar source process can be best explained by rupture on a curved plane or sub-events crossing multiple fault interfaces.
- Source complexity may indicate stress or structure heterogeneity in subducted slabs.

Abstract

The 30 May 2015 Mw 7.9 Bonin earthquake, one of the largest and deepest earthquakes ever recorded by modern seismology, provides a unique opportunity to study the source process and physical mechanisms of deep-focus earthquakes. We develop a novel back-projection technique that allows source imaging in full three-dimensional space with a high depth resolution. Our results indicate an initial SW-NE bilateral source propagation followed by a northwest source extension. The multiple-source inversion reveals a two-step source process with propagating directions sub-perpendicular to each other, consistent with the 3D back-projection result. The spatial distribution and focal mechanisms of the sub-events cannot be modeled by a single planar rupture, which may display a curved rupture plane or sub-events crossing multiple fault interfaces. The complex source process can be best explained by stress or structure heterogeneity within the deep slab.

Plain Language Summary

We utilize a 3D back-projection method and multiple-source inversion method. We find that the Bonin earthquake does not rupture on a planar fault plane. Instead, the earthquake process can be best explained by rupture on a curved fault plane or sub-events crossing multiple fault interfaces. The variation of spatial distribution and focal mechanisms may indicate the slab heterogeneity.

1 Introduction

Since deep-focus earthquakes were first discovered in the 1920s, the physics of deep-focus earthquakes is still under debate. Deep-focus earthquakes cannot be facilitated by the brittle-frictional processes like their shallow counterparts, because increasing pressure and temperature with depth strongly promotes ductile deformation and precludes brittle failure (Scholz, 2002). Various hypotheses have been proposed to explore the seismogenic mystery of deep-focus earthquakes. Two physical mechanisms, transformational failure and shear thermal instability, are widely considered as candidates to induce deep-focus ruptures. The transformational faulting mechanism assumes that metastable olivine wedges exists in subducted slabs. Phase transformation with volume shrink and heat release probably leads to an abrupt breakdown of the meta-stable olivine (Green, 2007; Green & Houston, 1995; Houston, 2015; Kirby, 1987; Wang et al., 2017). Liu & Zhang (2015) proposed that differential volume changes between the crust and mantle lithosphere is able to cause shear strain accumulation to trigger or induce deep earthquakes. Shear thermal instability hypothesizes that a non-linear positive feedback between temperature-dependent rheology and shear heating promotes shear localization that is able to achieve a catastrophic earthquake failure (Hobbs & Ord, 1988; Karato et al., 2001; Kelemen & Hirth, 2007; Ogawa, 1987; Kanamori et al., 1998; Prieto et al., 2013).

Previous investigations provided important constraints on source processes and physical mechanisms of deep-focus earthquakes. The fault plane orientation analysis of deep-focus earthquakes exhibited a complex rupture system of deep-focus earthquakes with both sub-horizontal and sub-vertical fault planes in the Tonga, Japan-Kuril-Kamchatka and Izu-Bonin-Mariana subduction zones, suggesting that local stress fields may control the fault plane orientation (Myhill & Warren, 2012; Warren et al., 2015; Warren et al., 2007). The source dimensions of some large earthquakes were proposed to extend out of the geometry of the meta-stable olivine zones (Chen & Wen, 2015; Chen et al., 2014; Silver et al., 1995; Wiens et al., 1994; Zhan et al., 2014a). However, Chen et al. (1995) suggested that the 1994 Mw 8.2 Bolivia earthquake could be interpreted as *En echelon* faults that could be fitted into the metastable olivine zone. Rupture parameters are important for understanding deep earthquake physics. Ye et al. (2016a) reported diverse rupture parameters for the 2015 Peru deep earthquake doublet, indicating different physical mechanisms. Ruiz et al. (2017) proposed that the doublet do not show significant different rupture parameters. It is also crucial for determining the detailed source process whether deep-focus earthquakes fail on a rupture plane (Antolik et al., 1996; 1999; Ye et al., 2013), several asperities (Silver et al., 1995; Wei et al., 2013; Zhan et al., 2014a) or different rupture planes triggering each other (Chen & Wen, 2015; Chen et al., 2014). In summary, different observations resulted in different conclusions. Elaborate analyses are needed to further constrain deep-focus earthquakes.

The recent 2015 Bonin earthquake (Fig. 1a) is the third largest deep-focus events ever recorded. It can provide a unique opportunity to investigate the source properties and dynamics, physical mechanisms of large deep-focus earthquakes, and even the seismic structure of the Izu-Bonin slab. The earthquake is reported with a moment magnitude of Mw 7.9 and a depth of 677 km by the Global Centroid Moment Tensor (GCMT) solutions. The USGS slab 1.0 model (Hayes et al., 2012) and the tomography results (Fukao & Obayashi, 2013) showed that the Pacific slab subducts to the west beneath the Asian plate, and the International Seismological Centre (ISC) EHB seismicity (Engdahl et al., 1998) above 600 km is well consistent with these models (Figs. 1b, 1c). However, the Bonin earthquake is below the assumed slab illuminated by the background seismicity (Fig. 1c). An important approach to distinguishing the physical mechanism is if the earthquake occurred in the core of the slab (Silver et al., 1995; Wiens et al., 1994). The slab morphology is unclear and controversial as the previous studies reported (Obayashi et al., 2017; Okal & Kirby, 2016; Porritt & Yoshioka, 2016; Takemura et al., 2016; Yang et al., 2017; Ye et al., 2016b; Zhao et al., 2017). Those studies tried to explain why the 2015 Bonin earthquake is unusually deep and isolated from the background seismicity (Figs. 1b, 1c). Zhao et al. (2017) conducted P-wave tomography and suggested that the earthquake occurred within the subducting Pacific slab penetrating into the lower mantle without buckling. Kuge (2017) reported the earthquake occurred below 660-km discontinuity. Obayashi et al. (2017) suggested a shoe-shaped stagnant slab, and the 2015 event occurred in the heel part of this shoe-shaped slab. Porritt & Yoshioka (2016) observed multiple conversions from receiver functions within and below the transition zone, and proposed slab pileup in the mantle transition zone. Yang et al. (2017) proposed that the 2015 Bonin event could be explained by the slab buckling. Okal & Kirby (2016) recommended that the 2015 event occurred in a detached and fragmented slab. Although the slab geometry is still unclear, Takemura et al. (2016) examined propagation characteristics of P waves for the Bonin earthquake and compared them with the synthetics simulated with the earthquake located at the top, middle and bottom of the slab. They conclude that the Bonin earthquake occur at the bottom of the slab. The occurrence at the bottom of the slab is not consistent with the metastable-olivine wedge. Finite-fault inversion with a single fault plane was applied to study the earthquake (Ye et al., 2016b). The work was based on a source model derived with a simplified planar fault plane. Tomography and dynamic simulation of the slab geometry and dynamics displayed the complex morphology in the slab (Obayashi et al., 2017; Porritt & Yoshioka, 2016; Yang et al., 2017; Zhao et al., 2017). Structural and stress heterogeneity of the slab may result in source geometrical complexity. Therefore, we re-investigate the earthquake with more detailed analyses.

We apply a new 3D back-projection (3DBP) and our multiple-source inversion (MSI) to study the spatio-temporal distribution and focal mechanism of the sub-events, and constrain the three-dimensional source geometry and kinematic rupture process of the 2015 Bonin earthquake. Our study displays a non-planar spatial distribution and focal mechanisms of the sub-events. The variation of focal mechanisms along the location can be explained by either rupture on a curved fault plane or sub-events crossing multiple sub-parallel fault interfaces. The result can be explained by the slab stress or structure heterogeneity.

2 3D Back-projection

Back projection (BP) has been recognized as an important observational approach to imaging large deep earthquakes at teleseismic distance (e.g. Ishii et al., 2005). Deep earthquake waveforms are typically simpler than their shallow counterparts as the velocity structure near the source is less heterogeneous at depth (e.g., Frohlich, 2006), which allows BP imaging of more coherent wavefields at higher frequencies than previously achieved in BP studies of shallow earthquakes (Meng et al., 2014). In our previous work, the BP imaging of the 2013 Mw 8.3 Okhotsk earthquake allowed for comparison of the rupture with local geometry of the subducting Pacific slab and evaluated the contributions of different physical mechanisms in a single earthquake (Meng et al., 2014).

A key limitation of the standard back-projection approach is the lack of depth resolution. Since a trade-off of source location and timing exists along the ray-path of the seismic wave, a predefined fault plane is thus required to reduce the spatial uncertainty. At teleseismic distance, the seismic rays travel almost vertically. The BP usually achieves good resolutions on sub-horizontal fault planes such as the shallow-dipping subduction interfaces. However, in the case of the sub-vertical fault planes, the location trade-off remains significant, as the fault plane is sub-parallel to the ray-path. In other words, the BP method usually provides a better horizontal resolution than the depth resolution, similar to that of the earthquake location problems. One recent development in BP imaging improves the depth resolution by combining multiple seismic phases. These phases intersect in space such that it overcomes the trade-offs of individual rays. Kiser et al. (2011) developed a modified BP approach to study the mechanisms of intermediate-depth earthquakes. The direct P phase and depth pP and sP phases are included in the back-projection analysis, which has potential to determining the energy distribution with respect to the depth and time. This capability of 3D imaging is also important to accurately estimate the rupture speeds. In conventional 2D imaging, since the orientations of fault planes need to be assumed, the source dimension is projected on the fault plane. An incorrected depth would cause the trade-off of source occurring time, and the wrong choice of the fault plane may lead to a very large uncertainty of the rupture speed. Here, we further develop a full-3D back-projection (3DBP) approach that resolves source locations in 3D volume.

Taking advantage of the recently developed large regional seismic arrays, we are able to image the source process by back-projecting the teleseismic data recorded by the Australian (AU), European (EU) and North American (NA) networks (Fig. 1a). For both direct P and pP phases, the seismograms are filtered between 0.25 to 1 Hz, the highest frequency band with adequate signal to noise ratio and waveform coherency. We align the initial P-wave and pP-wave arrivals (Figs. S1, S2) separately with a multi-channel cross-correlation technique (VanDecar & Crosson, 1990). For the BPs of both phases, we adopt a 10-s long sliding window to balance the temporal resolution and robustness. For each phase, we normalized the seismograms by their initial arrivals so that the waveforms have a uniform amplitude at all stations. This procedure removes the path and site effect on the waveform amplitude since the BP is based solely on the coherent phase information.

To fix the absolute location, the first arrival is assumed to come from the National Earthquake Information Center (NEIC) hypocenter location (140.49 °E, 27.83 °N, a depth of 677 km). Two independent BP processings of the P and pP phases determine 3D locations of the later high frequency (HF) sources based on the differential travel time relative to the hypocenter. The BP of the two phases are first normalized by their peak power within each time frame and are then summed up to combine the resolutions of the two phases. This normalization ensures equal weighting on both phases regardless their amplitude differences that are affected by the attenuation effect. The relative strength of each source is represented by the sum of beamforming power of the P wave and pP wave with equal weight to reflect energy signatures of the earthquake.

Our 3DBP suggests that the source process can be reliably imaged in the first 20s of the 2015 Bonin earthquake. The 3DBP spatio-temporal histories of the HF radiation of the Mw 7.9 mainshock imaged with the AU array, EU array and NA array are presented in Figs. 2, S3 and S4, respectively. We consider the 3DBP result using the AU array to be more confident, because the take-off angles of P and pP phases from the EU array are close to the nodal planes (Figs. S5a, S5b), and the radiation patterns further indicate that the amplitudes (hence the signal to noise ratio) of both P and pP phases of the AU array are significantly larger than that recorded by the EU and NA arrays (Fig. S5c). The size of the HF rupture is on the order of 40 km horizontally and 20 km in depth, rather compact compared to shallow earthquakes of similar magnitudes. The speed of the HF migration was overall slow, at approximately 2 km/s. The earthquake comprised two stages according to its rupture directions. In the first stage, the rupture began with a sub-horizontal propagation in the first 10 s, following a linear path bilaterally in the NE-SW direction. This pattern is clearly imaged by the AU array but is less prominent in the images produced with the EU and NA arrays (Figs. 2, S3, S4). In the second stage, a strong NW propagation took over and produced the dominant directivity (Fig. 2). The focal depth at this stage becomes shallower as the rupture propagates northwestward (Fig. 2). Such vertical propagation is generally consistent with the shallow dip angle of 26˚ of sub-horizontal plane inferred by GCMT (Fig. 2b). This two-step source propagation is consistent with the locations inverted using multiple-source inversion (stars in Fig. 2, introduced in section 3).

One concern of the 3DBP is whether the trade-off between horizontal locations and depths result in a large spatial uncertainty. These error bounds at each time step can be determined by bootstrapping the back-projections with random noise added to the signal. The noise level can be estimated based on the incoherent part of the waveforms. First, a reference point-source location in each snapshot is defined by the peak of the back-projection image. At each time step, seismograms are then aligned and stacked with the time shift predicted by the reference location. The noise at each station is computed as the waveform residual with respect to the array stacked waveforms. The noise is shuffled by randomizing its Fourier phase spectrum, then added back to the original waveforms. Note that the time shift is designed to estimate the incoherent noise and is not applied to the original waveforms. One hundred synthetic realizations of the stacked array recordings plus noise are then back-projected at each time step. The ellipsoids in Fig. 2 show the 95% confidence bound on the true peak location. Another source of the location uncertainty comes from the variation of the path effects. BP relies on the hypocenter time-correction to calibrate the travel time error due to 3D Earth structure. If there are substantial structural variations near the source domain, the hypocenter time-correction may be less valid to be applied to a distant sub-source away from the hypocenter. In order to assess such uncertainty of 3DBP in full 3D space, we conduct a resolution test using a M5.5 and a M6.0 deep-earthquake near the Bonin mainshock (Kiser & Ishii, 2013). These two earthquakes are approximately 150 km horizontally and 50 km vertically apart from each other. We back-project the two events using the timing correction evaluated at the M6.0 hypocenter. We then image the M5.5 event with respect to the M6.0 event and compare its BP-inferred location (peak of the BP kernel) with the catalog location. Figure S6 indicates that the difference between the BP and catalog location of M5.5 event is on the order of 15 km, considerably smaller than the source dimension of the mainshock. The location uncertainty due to path effect grows if the sub-source is further away from the hypocenter. Since the spatial separation from the two earthquakes are larger than the source dimension of the Bonin earthquake, we expect 15 km as the upper bound of the location uncertainty due to the path effect.

To further understand the performances of our 3DBP resolving complicated kinematic sources, we also conduct earthquake scenarios involving bilateral ruptures forming L-shape branches. This scenario is inspired by sub-event locations imaged by multiple-source inversions (section 3). We use seismic waveforms of a M6.5 deep earthquake (2015-06-23 12:18:30 UTC) that occurred in the Bonin area as empirical Green's functions (Figs. S7, S8). We adopt the seismograms recorded by the NA array which have high signal-to-noise ratio and adequate coherence. We create two rupture scenarios comprising 3 moving sources with a sub-event time interval of 5 s, and 5 moving sources with a time interval of 2.5 s, to represent discrete and more continuous ruptures, respectively. We back-project the synthetic seismograms at two frequency bands, from 0.25 Hz to 1 Hz with a window length of 10 s, the same processing parameters as used in the mainshock, and a higher frequency band of 0.5 to 2 Hz with a window length of 5 s. According to Fig. S9, 3DBP is overall capable of resolving the spatio-temporal pattern of the input source. In the case of the continuous sources, 3DBP reasonably reproduces the rupture extension, timing and sub-event locations (Fig. S9a). For the discrete sources, 3DBP almost identically recovers the input source at the frequency range of 0.25 Hz to 1 Hz (Fig. S9b). The higher-frequency (0.5 - 2 Hz) result is slight noisier and shows more scatters, possibly due to the smaller waveform coherency. Note that the BPs of the discrete sources at both frequency bands produces minor connections between the first and second sub-events. This is because the window length is comparable with or longer than the temporal separations between sub-events, so that a single window includes multiple sub-events. Overall, the synthetic tests demonstrate that 3DBP is capable of imaging the input kinematic scenarios.

3 Multiple-source inversion

To analyze the spatio-temporal distribution and focal mechanisms of energy packets of the seismograms, we adopt a multiple-source inversion method to invert the direct and near-surface reflected waveforms (Chen et al., 2014; Chen & Wen., 2015). Our MSI method makes no a prior assumption on the focal mechanism of source energy in waveform modeling and is capable of resolving the focal mechanism change during the earthquake. The MSI method also combines the direct and near-surface reflected phases as seismic constraints, and resolves the depth distribution of the seismic energy during a large earthquake (which previous studies always assumed on a plane). The two unique aspects enabled us to discover that the geographic distribution of the sub-events during some deep earthquakes does not fit into a rupture plane and the sub-events during some large deep earthquakes exhibit changing focal mechanisms, providing fresh insights into the physical mechanisms of deep earthquakes (Chen & Wen, 2015).

The method simultaneously infers focal mechanism (*strike*, *dip* and *slip*), centroid time from the origin time (*dt*), centroid location (*dn*, *de* and *dz*) from the hypocenter, seismic moment, and seismic duration (duration of a half-sine function) for each sub-event. Seismic Green's functions are computed by the Generalized Ray Theory method (Helmberger, 1968), based on the velocity and attenuation structures of Preliminary Reference Earth Model (PREM) (Dziewonski and Anderson, 1981). We utilize the simulated heat-annealing algorithm to search the model parameters through minimizing the misfits between seismic data and synthetic waveforms (Chen et al., 2014; Ji et al., 2002).

To align the waveforms correctly, we high-pass filter the P-wave data above 1 Hz and determine the first arrival onsets. The first P arrival onsets are clearly identified in the high frequency band of 1 to 4 Hz. We initially pick SH, pP and sSH arrival onsets based on PREM (Dziewonski & Anderson, 1981). We perform iterative inversion starting with P wave heavily weighted, and then adjust the alignments of pP, SH and sSH waves to best match synthetics and data during the inversions (Chen & Wen, 2015).

The earthquake begins with strong sub-events during the first ~ 15 s, followed by a weak energy release lasting ~ 5 s. We utilize an L-curve to demonstrate that five sub-events can reasonably fit the seismograms (Fig. S10a). The seismic energy exhibits five move-outs discernible in the vertical P-seismograms (Fig. S10b). Based on those move-outs, we can preliminarily identify the five sub-event propagating directions and the initial locations for the inversion. We adopt searching ranges as ±20 km from the initial locations. The MSI result exhibits that the first sub-event is to the northeast of the initiation point (the azimuth with the earliest arrival of the P waves). The second and third sub-events are to the south and the southwest, respectively. The fourth and fifth sub-events propagate to the northwest. The inferred best-fitting sub-events are shown in Fig. 3a (red beach balls) and Table S1. The MSI results in reasonably good waveform fitting between synthetics (red traces in Figs. 3b, S11) and seismic data (black traces in Figs. 3b, S11) for P, pP, SH and sSH waves. The inverted sub-events align closed to the GCMT sub-horizontal fault plane as a flipped ‘T’ shape (stars in Fig.2, red dots in Fig. 3a), well consistent with the AU back-projection result (ellipsoids in Fig. 2). The first three sub-events propagate bilaterally in the direction NE-SW with moment magnitudes of ~ 7.5, while the fourth and fifth sub-events propagate to northwest sub-perpendicular to the first three sub-events, with moment magnitudes of 7.5 and 7.1, respectively. The focal mechanisms (strike/dip/rake) of the sub-events are 47/25/329, 40/30/321, 30/29/316, 21/22/310 and 10/14/308, respectively. The summed moment tensor of the inferred sub-events yields an overall focal mechanism of 35/26/321, almost identical to the GCMT solution (37/26/322) of the mainshock. The predicted seismic moment is 7.1×10^{20} N m, slightly lower than 7.7×10^{20} N m in the GCMT solution. We also found that the sub-event strike and dip angles decrease as it moves away from the first sub-event.

We perform resolution tests using the same source and receiver configuration (Figs. 1a, 3a, Table S1). The first test is to invert the noise-free synthetic data. We perform the MSI for 50 times with random initial parameters within the searching ranges in the real data inversion, and obtain the standard deviation error for each parameter as the uncertainty (Chen & Wen, 2015). The uncertainties of the *strike*, *dip*, *slip*, source duration, moment, *dt*, *dn*, *de*, *dz* for the five sub-events are shown in Table S2. The strike uncertainties are less than 5˚, the dip uncertainty less than 2˚, and the location uncertainty less than 3˚. The later three sub-events are overlapped with each other, leading to trade-offs of the parameters, especially source durations and locations. The fifth sub-event has a relatively smaller magnitude, therefore, it weighs less during the inversion. The second test is to invert the synthetic data with increasing real noise. We truncate the real noise before the P wave arrivals and normalize it to 0 - 100% of the maximum amplitude of the data. The uncertainties naturally increase with the noise amplitudes (Fig. S12). The uncertainties would not lead to misinterpretation of our result until the noise level reach 80% of the maximum amplitudes of the data. The uncertainties are shown in Table S3. The strike uncertainties are less than 8˚, the dip uncertainties less than 5˚, and the location uncertainties less than 4 km. Because of the non-linear characteristics of waveform inversion, we apply the bootstrapping method to evaluate the inversion uncertainties from geometry of the seismic stations. We randomly resample 72 channels (80%) from the 90 used channels. We perform 50 times with random initial parameters as above. The strike uncertainties are less than 8°, the dip uncertainties less than 4°, and the location uncertainties less than 5 km (Table S4). We plot the location uncertainties with the GCMT fault planes in Fig. 4a. The three radii for each event (Fig. 4a) represent the uncertainties for x, y and z directions (Table S4). We show that the events are not tangent to the fault planes; therefore, they do not rupture on the plane. We plot the focal mechanisms and their uncertainties (blue circles) in 3D space and the GCMT fault planes for reference (Figs. 4b, 4c). The figures exhibit that focal mechanisms of the fourth and fifth sub-events deviate from the GCMT solution, more than 20° for the strike and 10° for the dip. The deviations are larger than the inversion uncertainties (Table S4). The result suggests that the source process is not on a planar fault rupture.

Previous study suggested a planar rupture for the earthquake (Ye et al., 2016b). To exclude the misinterpretation from the inversion uncertainty, we perform planar model tests to examine if the fitting of seismic data can be compelled onto a single fault plane. The normalized data misfits for the inversions are presented in Fig. 3c. Our first test is to check if the locations and focal mechanisms of the sub-events can be compelled onto the GCMT sub-horizontal focal plane with the strike of 37° and the dip of 26°. The inferred sub-event model is shown in Fig. 3a (blue beach balls) and Table S5. The normalized data misfit of the best-fitting model (red trace in Fig. 3c) is convincingly smaller than that of the sub-horizontal plane model (blue trace in Fig. 3c). The best-fitting model (red traces in Fig. S11) produces better fitting timings and amplitudes of the seismic waveforms than the sub-horizontal plane model. The most notable misfits are the amplitudes at some particular waveforms, such as the P waves at stations GNI, BRVK, KONO, KBS, the S waves at stations COLA, COR and JOHN (blue traces in Figs. 3b, S11), because the sub-events are prescribed to the strike and dip of the GCMT sub-horizontal plane.

The second test is to compel the sub-events onto the GCMT sub-vertical plane with the strike of 162° and the dip of 74°. The normalized data misfit of the sub-vertical plane model (black trace 2 in Fig. 3c) is even larger than that of the sub-horizontal plane model (blue trace in Fig. 3c). The synthetics predicted by the inferred model (Fig. S13, Table S6) cannot match the seismic data in both arrival times and amplitudes of the sub-events (Fig. S14), because the energy packets are prescribed to propagate on the assumed sub-vertical rupture plane that the predicted energy associated with the first and third sub-events would not match the azimuthal variations of the arrival times in the P and pP observations. To fit the data, the seismic source for the first sub-event is required to move southwest, and the third sub-event to the northeast (Fig. S13). The mismatches of arrival times are evident in P waveforms at stations UOSS, GNI, MAKZ, BRVK, KONO and KBS, and in pP waveforms at stations TAU, NWAO, MBWA, MSEY and UOSS. The misfits of amplitudes are obvious in P waveforms at stations KAPI and MSEY, and in S waveforms at stations COLA, COR, JOHN, CTAO, TAU, WRAB and KAPI (Fig. S14).

The third test is to invert a new fault plane that can best match the waveforms. We compel all the sub-events onto the new fault plane. Therefore, we invert the fault plane location and orientation for all the sub-events, and the rake angle for each sub-event. The result shows that the strike of 36.5° and the dip of 26.5° can best match the time arrival and radiation pattern, consistent with the GCMT sub-horizontal plane. The normalized data misfit of the sub-horizontal plane model (blue trace in Fig. 3c) is almost the same as that of the best planar model (purple trace in Fig. 3c). The best plane model can be referred to the model in the first test (blue beach balls in Fig. 3a, Table S1). The synthetics can be referred to the blue traces in Figs. 3b and S11. The test demonstrates that the GCMT sub-horizontal plane model is the best planar model for this event, consistent with the previous study (Ye et al., 2016b). However, a curved rupture plane, or sub-events crossing multiple fault interfaces can better explain the result.

4 Discussion

Our case study of the Bonin earthquake indicates the importance of studying the deep earthquake source process in full 3D space with 3DBP and MSI that include both the direct and depth phases. The depth information is particularly useful to constrain the geometry of deep earthquakes. For example, the 2013 Mw 8.3 Okhotsk earthquake was first considered to be confined on the GCMT sub-horizontal plane (Meng et al., 2014; Wei et al., 2013; Ye et al., 2013). However, the inversion with the direct waves and the near-surface reflected waves exhibited that the earthquake propagated to the southwest with a downdip extension, which is inconsistent with either the GCMT sub-horizontal or sub-vertical planes (Chen et al., 2014). Chen & Wen (2015) utilized the depth phases to constrain the global large-deep focus earthquakes and suggested non-planar features for some of those earthquakes. Kiser et al. (2011) studied intermediate-depth earthquakes with the pP and sP phases and proposed large depth extensions for some intermediate-depth earthquakes. Ruiz et al. (2017) employed both downgoing teleseismic P phases and upgoing regional P phases to provide high-resolution depth constraints for the Peru doublets, while Ye et al. (2016a) used teleseismic phases only. Those studies indicate that employing the depth phases is crucial for deciphering source processes of deep earthquakes. We apply our 3DBP using seismic data recorded from the AU, EU and US arrays. The 3DBP results display sort of discrepancy among the results using the three arrays. The result using the AU array unravels a bilateral source extension in the NE-SW direction in the first 10 s, while the results using the EU and US arrays do not prove the same feature. We quantitatively study the radiation pattern of the earthquake and find that seismograms recorded by the AU array are stronger and therefore more reliable. The result using the AU array is consistent with our multiple-source inversion result. We suggest that a quantitative investigation of the radiation pattern is crucial for comparison of the results using different seismic arrays.

MSI exhibits the similar spatio-temporal pattern as 3DBP does. The sub-events do not align on either of the GCMT planes. We note that seismic attenuation and heterogeneity would generate systematical bias of the absolute location; however, our result is based on relative timings, which can minimize the errors from the attenuation and heterogeneity (Chen et al., 2014). The near-source structures of multiple faults may potentially add to the waveform complexity and decrease the waveform coherence among the four quadrants of the focal sphere. This is not the case for the Bonin earthquake since the seismic waveforms of this earthquake are consistent in all four quadrants, and are reasonably fit by synthetics. MSI can also determine focal mechanisms of the sub-events, which gives rise to better understanding of the source complexity than previous studies (e.g. Ye et al. 2016b). In the case of the Mw 8.3 Okhotsk earthquake mentioned above, Chen et al. (2014) determined focal mechanisms of the sub-events inconsistent with the source extension and suggested a cascading failure during the earthquake. In this study, the earthquake can be modeled by five sub-events based on reasonably good fitting of the seismic P, pP, S and sS waveforms. The MSI reveals focal-mechanism variations of the sub-events, indicating that the earthquake cannot be modeled by a single planar rupture. Our inverted source process is generally consistent with Ye et al. (2016b), but reveals information that is more detailed. We compare the MSI results of the Okhotsk earthquake and the Bonin earthquake. The Okhotsk earthquake has a relatively larger magnitude, and a significant depth extension. The focal mechanisms of those sub-events are inconsistent with their spatial distribution; therefore, the Okhotsk earthquake cannot be explained by one or two ruptures (Chen et al. 2014). This Bonin earthquake has a relatively smaller magnitude. The spatio-temporal distribution and focal mechanisms of the sub-events vary slightly, but are still close to the GCMT sub-horizontal fault plane. Such spatially variable focal mechanisms within one earthquake may be explained by continuous rupture along a single curved fault interface or sub-events crossing multiple sub-parallel fault planes (Cai & Wiens, 2016; Chen & Wen, 2015; Poli et al., 2016). In the former case, focal mechanisms varying along the location are consistent with a curved rupture process (Figs. 4b, 4c, Table S1). The curvature required for the single fault plane is about $1x10^{-5}$ m^{-1},.which is not abnormal for fault surface traces (Bergbauer, 2004; Mynatt et al., 2007), but whether such curvature exist for deep-focus rupture remains to be verified. In the latter case, multiple sub-parallel faults with moderately varying strikes could be connected in a single macroscopic rupture with step over on rupture propagation. The required step-over distance between the sub-faults are in the order of 10 km, which is a comfortable step-over distance given a seismogenic width of 50 km (Bai & Ampuero, 2017). Such step-over distance is larger than typical spacing of 5 km found for shallow crustal earthquakes (Wesnousky, 2005), which is not surprising given a much larger seismogenic width expected for deep earthquakes. Multiple-parallel faults can also be explained by sub-events triggering each other (Chen et al., 2014; Chen & Wen, 2015; Poli et al., 2016).

Source propagating velocity is an important parameter for earthquake source process. It was reported to vary greatly (Frohlich, 2006; Suzuki & Yagi, 2011; Zhan et al, 2014b; Chen & Wen, 2015). Our 3DBP result reveals a low source propagating velocity of 2 km/s, approximately 0.3 times of S-wave velocity at the depth. Our result is consistent with the lower bound shown by Frohlich (2006) and less than 0.6Vs as Suzuki & Yagi (2011) exhibited. Chen & Wen (2015) suggested that variable source propagating velocities can be best explained by different triggering processes by the static or dynamic stress generated by the preceding sub-events. Our 3DBP and MSI results indicate that the earthquake has a duration of ~ 20 s with a moment of 7.1 x 10^{20} N m (Mw 7.9). The result is consistent with the moment-duration relationships in previous studies (Houston et al., 1998; Frohlich, 2006; Chen & Wen, 2015).

Our investigation indicates that the inverted sub-event focal mechanisms are generally consistent with the GCMT solution. The compressive stress axis is inconsistent with the downdip extension of the slab geometry (Zhao et al., 2017). The focal mechanisms vary along the location, which indicates strong heterogeneity in the slab, either stress heterogeneity (Yang et al., 2017) or varying pre-existing weak zones (Chen & Wen, 2015). The slab heterogeneity may be caused by slab stagnation, buckling, pileup and thickening near 660 km (Obayashi et al., 2017; Porritt & Yoshioka, 2016; Yang et al., 2017). Those processes can generate stress heterogeneities (Myhill, 2013; Poli & Prieto, 2016), and/or distort the preexisting weak zones to complex geometries, giving rise to sub-events of various focal mechanisms (Ruiz et al., 2017; Zahradnik et al., 2017). Such stress can trigger either phase transformation (Wang et al., 2017) or shear thermal instability (Ogawa, 1987). The step-over distance is a critical factor for the step-over model of sub-events crossing multiple fault interfaces. For shallow earthquakes, the seismogenic depth is limited by the thickness of the brittle crust (~10 km). For deep earthquakes, if the thermal shear instability is the driving mechanism, the seismogenic width is predicted to be 40 – 60 km (Karato et al., 2001), which is much larger than the metastable olivine wedge.

Acknowledgments

We thank editors and two anonymous reviewers for insightful and constructive comments and suggestions. The work is supported by NSF EAR 1214215 and NSF EAR 1614609. The seismic data are downloaded from the Incorporated Research Institutions for Seismology (IRIS) Data

Center (http://ds.iris.edu/ds/nodes/dmc/). The facilities of IRIS Data Services, and specifically the IRIS Data Management Center, were used for access to waveforms, related metadata, and/or derived products used in this study. IRIS Data Services are funded through the Seismological Facilities for the Advancement of Geoscience and EarthScope (SAGE) Proposal of the National Science Foundation under Cooperative Agreement EAR-1261681. The seismic waveforms are processed using SAC software. The figures are plotted by the GMT and Paraview. The 3DBP source code and the example of the Bonin earthquake is available in supplementary file 1. The MSI source code is currently unavailable due to the restrictive open source policy of the Los Alamos National Laboratory.

Reference

Antolik, M., Dreger, D., & Romanowicz, B. (1996). Finite fault source study of the great 1994 deep Bolivia earthquake. *Geophysical Research Letters*, **23**(13), 1589-1592, doi:10.1029/96gl00968.

Antolik, M., Dreger, D., & Romanowicz, B. (1999). Rupture processes of large deep-focus earthquakes from inversion of moment rate functions. *J. Geophys. Res.-Solid Earth*, **104**(B1), 863-894, doi:10.1029/1998jb900042.

Bai, K., & Ampuero, J.-P. (2017). Effect of Seismogenic Depth and Background Stress on Physical Limits of Earthquake Rupture Across Fault Step Overs. *Journal of Geophysical Research: Solid Earth*, **122**(12), 10,280-210,298, doi:10.1002/2017JB014848.

Bergbauer, S. (2004). The use of curvature for the analyses of folding and fracturing with application to the Emigrant Gap anticline, Wyoming. (Doctoral Dissertation), Stanford University.

Cai, C., & Wiens, D. A. (2016). Dynamic triggering of deep earthquakes within a fossil slab. *Geophysical Research Letters*, **43**(18), 9492-9499, doi:10.1002/2016GL070347.

Chen, W. P. (1995). En-echelon rupture during the great Bolivian earthquake of 1994. *Geophysical Research Letters*, **22**(16), 2261-2264, doi:10.1029/95gl01805.

Chen, Y., & Wen, L. (2015). Global large deep-focus earthquakes: Source process and cascading failure of shear instability as a unified physical mechanism. *Earth Planet. Sci. Lett.*, **423**, 134-144.

Chen, Y., Wen, L., & Ji, C. (2014). A cascading failure during the 24 May 2013 great Okhotsk deep earthquake. *J. Geophys. Res.-Solid Earth*, **119**(4), 3035-3049, doi:10.1002/2013jb010926.

Dziewonski, A. M., & Anderson, D. L. (1981). Preliminary reference Earth model. *Physics of the Earth and Planetary Interiors*, **25**(4), 297-356, doi:10.1016/0031-9201(81)90046-7.

Engdahl, E.R., van der Hilst, R., & Buland, R. (1998). Global teleseismic earthquake relocation with improved travel times and procedures for depth determination, Bull. Seism. Soc. Am. 88, 722-743.

Frohlich, C. (2006), Deep earthquakes, Cambridge university press.

Fukao, Y., & Obayashi, M. (2013). Subducted slabs stagnant above, penetrating through, and trapped below the 660 km discontinuity. *Journal of Geophysical Research: Solid Earth*, **118**(11), 5920-5938, doi:10.1002/2013JB010466.

Green, H. W. (2007). Shearing instabilities accompanying high-pressure phase transformations and the mechanics of deep earthquakes. *Proceedings of the National Academy of Sciences of the United States of America*, **104**(22), 9133-9138, doi:10.1073/pnas.0608045104.

Green, H. W., & Houston, H. (1995). The mechanisms of deep earthquakes. *Annual Review of Earth and Planetary Sciences*, **23**, 169-213, doi:10.1146/annurev.ea.23.050195.001125.

Hayes, G. P., Wald, D. J., & Johnson, R. L. (2012). Slab1.0: A three-dimensional model of global subduction zone geometries. *J. Geophys. Res.-Solid Earth*, **117**, 15, doi:10.1029/2011jb008524.

Helmberger, D.V. (1968). The crust-mantle transition in Bering sea. Bulletin of the Seismological Society of America 58, 179-214.

Hobbs, B. E., & Ord, A. (1988). Plastic instabilities - implications for the origin of intermedite and deep focus earthquakes. *Journal of Geophysical Research-Solid Earth and Planets*, **93**(B9), 10521-10540, doi:10.1029/JB093iB09p10521.

Houston, H. (2015). *Deep earthquake, Second Edition. Treatise on geophysics*, Elservier.

Houston, H., Benz, H., & Vidale J. (1998). Time functions of deep earthquakes from broadband and short-period stacks. *J. Geophys. Res.-Solid Earth*, **103**, B12, doi:10.1029/98JB02135.

Ishii, M., P. M. Shearer, H. Houston, and J. E. Vidale (2005), Extent, duration and speed of the 2004 Sumatra–Andaman earthquake imaged by the Hi-Net array, Nature, 435, 933, doi:10.1038/nature03675

Ji, C., Wald, D. J., & Helmberger, D. V. (2002). Source description of the 1999 Hector Mine, California, earthquake, part I: Wavelet domain inversion theory and resolution analysis. *Bulletin of the Seismological Society of America*, **92**(4), 1192-1207, doi:10.1785/0120000916.

Kanamori, H., Anderson, D. L., & Heaton, T. H. (1998). Frictional melting during the rupture of the 1994 Bolivian earthquake. *Science*, **279**(5352), 839-842, doi:10.1126/science.279.5352.839.

Karato, S., Riedel, M. R., & Yuen, D. A. (2001). Rheological structure and deformation of subducted slabs in the mantle transition zone: implications for mantle circulation and deep earthquakes. *Physics of the Earth and Planetary Interiors*, **127**(1-4), 83-108, doi:10.1016/s0031-9201(01)00223-0.

Kelemen, P. B., & Hirth, G. (2007). A periodic shear-heating mechanism for intermediate-depth earthquakes in the mantle. *Nature*, **446**(7137), 787-790, doi:10.1038/nature05717.

Kirby, S. H. (1987). Localized polymorphic phase-transformation in high-pressure faults and applications to the physical-mechanism of deep earthquakes. *Journal of Geophysical Research-Solid Earth and Planets*, **92**(B13), 13789-13800, doi:10.1029/JB092iB13p13789.

Kiser, E., Ishii, M., Langmuir, C. H., Shearer, P. M., & Hirose, H. (2011). Insights into the mechanism of intermediate-depth earthquakes from source properties as imaged by back projection of multiple seismic phases. *J. Geophys. Res.-Solid Earth,* **116**, doi:10.1029/2010jb007831.

Kiser, E., & Ishii, M. (2013). Hidden aftershocks of the 2011 Mw 9.0 Tohoku, Japan earthquake imaged with the backprojection method. *J. Geophys. Res,* **118**(10), 5564-5576, doi:10.1002/2013JB010158.

Kuge, K. (2017), Seismic Observations Indicating That the 2015 Ogasawara (Bonin) Earthquake Ruptured Beneath the 660 km Discontinuity, Geophysical Research Letters, 44(21), doi:10.1002/2017GL074469.

Liu, L. J., & Zhang, J. S. (2015). Differential contraction of subducted lithosphere layers generates deep earthquakes. *Earth Planet. Sci. Lett.*, **421**, 98-106, doi:10.1016/j.epsl.2015.03.053.

Meng, L., Ampuero, J.-P., & Buergmann, R. (2014). The 2013 Okhotsk deep-focus earthquake: Rupture beyond themetastable olivinewedge and thermally controlled rise time near the edge of a slab. *Geophysical Research Letters,* **41**(11), 3779-3785, doi:10.1002/2014gl059968.

Myhill, R. (2013). Slab buckling and its effect on the distributions and focal mechanisms of deep-focus earthquakes. *Geophys. J. Int.*, **192**(2), 837-853, doi:10.1093/gji/ggs054.

Myhill, R., & Warren, L. M. (2012). Fault plane orientations of deep earthquakes in the Izu-Bonin-Marianas subduction zone. *J. Geophys. Res.-Solid Earth*, **117**, doi:10.1029/2011jb009047.

Mynatt, I., Bergbauer, S., & Pollard, D. D. (2007). Using differential geometry to describe 3-D folds. *Journal of Structural Geology*, **29**(7), 1256-1266, doi:10.1016/j.jsg.2007.02.006.

Obayashi, M., Fukao, Y., & Yoshimitsu, J. (2017). Unusually deep Bonin earthquake of 30 May 2015: A precursory signal to slab penetration? *Earth Planet. Sci. Lett.*, **459**, 221-226, doi:doi.org/10.1016/j.epsl.2016.11.019.

Ogawa, M. (1987). Shear instability in a viscoelastic material as the cause of deep-focus earthquakes. *Journal of Geophysical Research-Solid Earth and Planets*, **92**(B13), 13801-13810, doi:10.1029/JB092iB13p13801.

Okal, E., & Kirby, S. H. (2016), The large Bonin deep Event of 30 May 2015: Seismogenesis in a Detached and Fragmented Slab, paper presented at EGU General Assembly Conference Abstracts.

Poli, P., & Prieto, G. A. (2016). Global rupture parameters for deep and intermediate-depth earthquakes. *Journal of Geophysical Research: Solid Earth*, **121**(12), 8871-8887, doi:10.1002/2016JB013521.

Poli, P., Prieto, G., Rivera, E., & Ruiz, S. (2016). Earthquake initiation and thermal shear instability in the Hindu Kush intermediate depth nest, *Geophysical Research Letters*, **43**(4), 1537-1542, doi:10.1002/2015GL067529.

Porritt, R. W., & Yoshioka, S. (2016). Slab pileup in the mantle transition zone and the 30 May 2015 Chichi-jima earthquake. *Geophysical Research Letters*, **43**(10), 4905-4912, doi:10.1002/2016GL068168.

Prieto, G. A., Florez, M., Barrett, S. A., Beroza, G. C., Pedraza, P., Blanco, J. F., & Poveda, E. (2013). Seismic evidence for thermal runaway during intermediate-depth earthquake rupture. *Geophysical Research Letters*, **40**(23), 6064-6068, doi:10.1002/2013GL058109.

Ruiz, S., H. Tavera, P. Poli, C. Herrera, C. Flores, E. Rivera, & R. Madariaga (2017), The deep Peru 2015 doublet earthquakes. Earth Planet. Sci. Lett., 478, 102-109, doi:https://doi.org/10.1016/j.epsl.2017.08.036.

Scholz, C. H. (2002). *The mechanics of earthquakes and faulting*, Cambridge university press.

Suzuki, M., & Yagi, Y. (2011), Depth dependence of rupture velocity in deep earthquakes. *Geophysical Research Letters*, **38**, L05308, doi:10.1029/2011GL046807.

Silver, P. G., Beck, S. L., Wallace, T. C., Meade, C., Myers, S. C., James, D. E., & Kuehnel, R. (1995). Rupture characteristics of the deep Bolivian earthquake of 9 June 1994 and the mechanisms of deep-focus earthquakes. *Science*, **268**(5207), 69-73, doi:10.1126/science.268.5207.69.

Takemura, S., Maeda, T., Furumura, T., & Obara, K. (2016). Constraining the source location of the 30 May 2015 (M-w 7.9) Bonin deep-focus earthquake using seismogram envelopes of high-frequency P waveforms: Occurrence of deep-focus earthquake at the bottom of a subducting slab. *Geophysical Research Letters*, **43**(9), 4297-4302, doi:10.1002/2016gl068437.

VanDecar, J., & Crosson, R. (1990). Determination of teleseismic relative phase arrival times using multi-channel cross-correlation and least squares. *Bulletin of the Seismological Society of America*, **80**(1), 150-169.

Wang, Y., Zhu, L., Shi, F., Schubnel, A., Hilairet, N., Yu, T., Rivers, M., Gasc, J., Addad, A., & Deldicque, D. (2017). A laboratory nanoseismological study on deep-focus earthquake micromechanics. *Sci. Adv.*, **3**(7), e1601896.

Warren, L. M., Baluyut, E. C., Osburg, T., Lisac, K., & Kokkinen, S. (2015). Fault plane orientations of intermediate-depth and deep-focus earthquakes in the Japan-Kuril-Kamchatka subduction zone. *J. Geophys. Res.-Solid Earth*, **120**(12), 8366-8382, doi:10.1002/2015jb012463.

Warren, L. M., Hughes, A. N., & Silver, P. G. (2007). Earthquake mechanics and deformation in the Tonga-Kermadec subduction zone from fault plane orientations of intermediate- and deep-focus earthquakes. *J. Geophys. Res.-Solid Earth*, **112**(B5), doi:10.1029/2006jb004677.

Wei, S. J., Helmberger, D., Zhan, Z. W., & Graves, R. (2013). Rupture complexity of the M-w 8.3 sea of okhotsk earthquake: Rapid triggering of complementary earthquakes? *Geophysical Research Letters*, **40**(19), 5034-5039, doi:10.1002/grl.50977.

Wesnousky, S. G. (2005). The San Andreas and Walker Lane fault systems, western North America: Transpression, transtension, cumulative slip and the structural evolution of a major transform plate boundary. *Journal of Structural Geology*, **27**(8), 1505-1512, doi:10.1016/j.jsg.2005.01.015.

Wiens, D. A., McGuire, J. J., Shore, P. J., Bevis, M. G., Draunidalo, K., Prasad, G., & Helu, S. P. (1994). A deep earthquake aftershock sequence and implications for the rupture mechanism of deep earthuqakes. *Nature*, **372**(6506), 540-543, doi:10.1038/372540a0.

Yang, T., Gurnis, M., & Zhan, Z. (2017). Trench motion-controlled slab morphology and stress variations: Implications for the isolated 2015 Bonin Islands deep earthquake. *Geophysical Research Letters*, **44**(13), 6641-6650, doi:10.1002/2017GL073989.

Ye, L., Lay, T., Kanamori, H., & Koper, K. D. (2013). Energy Release of the 2013 Mw 8.3 Sea of Okhotsk Earthquake and Deep Slab Stress Heterogeneity. *Science*, **341**(6152), 1380-1384, doi:10.1126/science.1242032.

Ye, L., Lay, T., Kanamori, H., Zhan, Z. W., & Duputel, Z. (2016a). Diverse rupture processes in the 2015 Peru deep earthquake doublet. *Sci. Adv.*, **2**(6), 9, doi:10.1126/sciadv.1600581.

Ye, L., Lay, T., Zhan, Z. W., Kanamori, H., & Hao, J. L. (2016b). The isolated similar to 680 km deep 30 May 2015 M-w 7.9 Ogasawara (Bonin) Islands earthquake. *Earth Planet. Sci. Lett.*, **433**, 169-179, doi:10.1016/j.epsl.2015.10.049.

Zahradník, J., H. Čížková, C. R. Bina, E. Sokos, J. Janský, H. Tavera, and J. Carvalho (2017), A recent deep earthquake doublet in light of long-term evolution of Nazca subduction, Scientific Reports, 7, 45153, doi:10.1038/srep45153

Zhan, Z., Kanamori, H., Tsai, V. C., Helmberger, D. V., & Wei, S. (2014a). Rupture complexity of the 1994 Bolivia and 2013 Sea of Okhotsk deep earthquakes. *Earth Planet. Sci. Lett.*, **385**(0), 89-96, doi:http://dx.doi.org/10.1016/j.epsl.2013.10.028.

Zhan, Z.W., Helmberger, D.V., Kanamori, H., Shearer, P.M. (2014b). Supershear rupture in a M-w 6.7 aftershock of the 2013 Sea of Okhotsk earthquake. Science 345, 204-207, doi: 10.1126/science.1252717.

Zhao, D., Fujisawa, M., & Toyokuni, G. (2017). Tomography of the subducting Pacific slab and the 2015 Bonin deepest earthquake (Mw 7.9). *Scientific Reports*, **7**, 44487, doi:10.1038/srep44487

Figure captions

Figure 1. (a) Location of the 30 May 2015 earthquake (red star) and seismic station coverage. Purple circles represent seismic arrays used in 3D back-projection. Blue triangles represent seismic stations used in multiple-source inversion. Red beach ball describes the GCMT focal mechanism of the earthquake. (b) Map view of the seismicity at the adjacent region. The circles represent the seismicity, color-coded by depth. The depth contours labeled with slab depth are from the USGS slab 1.0 model (Hayes et al., 2012). The red star represents the location of the 2015 Bonin earthquake. (c) Cross-section view of the seismicity and tomography model (Fukao & Obayashi, 2013) along the rectangle AA' in (b). Red beach ball represents the mainshock focal mechanism projected in side view.

Figure 2. 3DBP image using the Australian (AU) network for the 2015 Mw 7.9 Bonin earthquake. (a) BP locations in map view. (b) Cross-section of BP images along OA in (a). (c) Cross-section of BP images along OB in (a). Inset map in (a) is normalized beamform power as a function of time. The colors and shapes of the ellipsoids demonstrate the 3DBP timing (with a interval of 1 s) and the 95% confidence interval on the peak locations. The red cross indicates the hypocenter location. The colors and shapes of the stars show the MSI inferred timing and location in Table S1 and Fig. 3 for the comparison.

Figure 3. (a) Locations of the best-fitting sub-event model (red points) and the sub-event model compelled onto the sub-horizontal plane (blue points), along with slab depth contours (black dashed traces). Red and blue beach balls represent inferred focal mechanisms of the sub-events of the best-fitting sub-event model (Table S1) and the best planar model (Table S5), labeled with the sub-event peak times/moment magnitudes/depths. (b) Selected seismograms (black traces) in four quadrants comparing with synthetics predicted based on the best-fitting sub-event model (red traces) and synthetics based on the sub-horizontal model (blue traces) in Fig. S11. Seismic records are labeled with station name, phase, along with azimuth, epicentral distance, and the maximum amplitude of the data. (c) The normalized data misfits of 500 iterations for the best-fitting (red), the sub-horizontal (blue), and the sub-vertical (black) models.

Figure 4. Non-planar (a) sub-event distribution, and (b) and (c) focal mechanisms of the sub-events. (a) Three-dimensional spatial distribution of inverted sub-events (red ellipsoids) labeled with their occurring sequence, along with the focal planes (gray planes) of the GCMT solutions. The three elliptic radii represent the location uncertainty in x, y and z directions (Table S4). (b) and (c) three-dimensional focal mechanisms shown in (b) the azimuth of 160° and the view angle of 30° and (c) the azimuth of 250° and the view angle of 10°. The yellow conjugate planes represent the GCMT fault planes for the comparison. The blue circles represent focal-mechanism uncertainty (Table S4) for the sub-events. Blue arrows highlight the focal-mechanism variations.

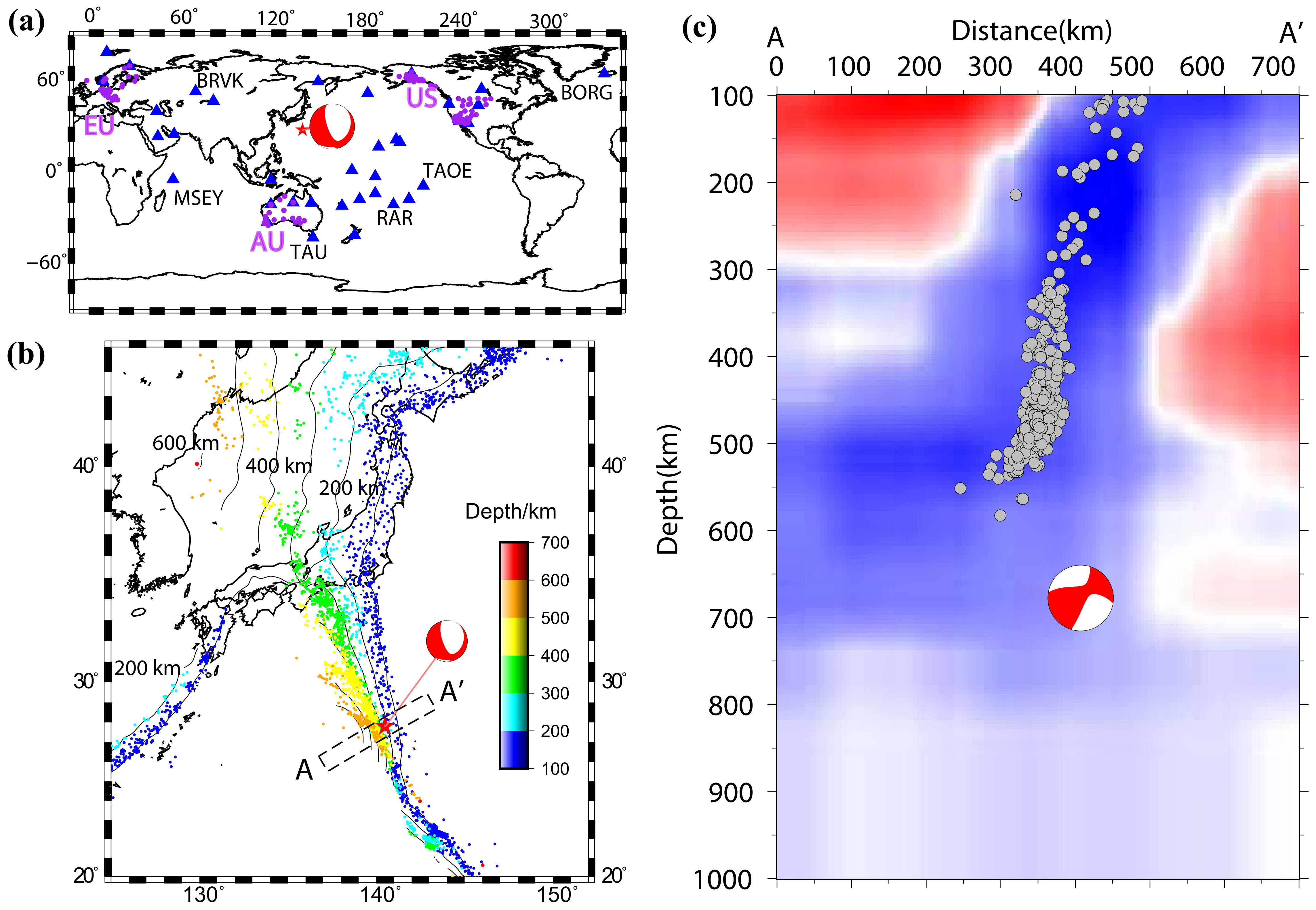

(a)
0°
60°
120°
180°
240°
300°
60°
0°
−60°
BRVK
EU
US
BORG
TAOE
MSEY
RAR
AU
TAU
(b)
600 km
400 km
200 km
200 km
Depth/km
700
600
500
400
300
200
100
A
A′
40°
30°
20°
130°
140°
150°
(c)
A
A′
Distance(km)
0
100
200
300
400
500
600
700
Depth(km)
100
200
300
400
500
600
700
800
900
1000

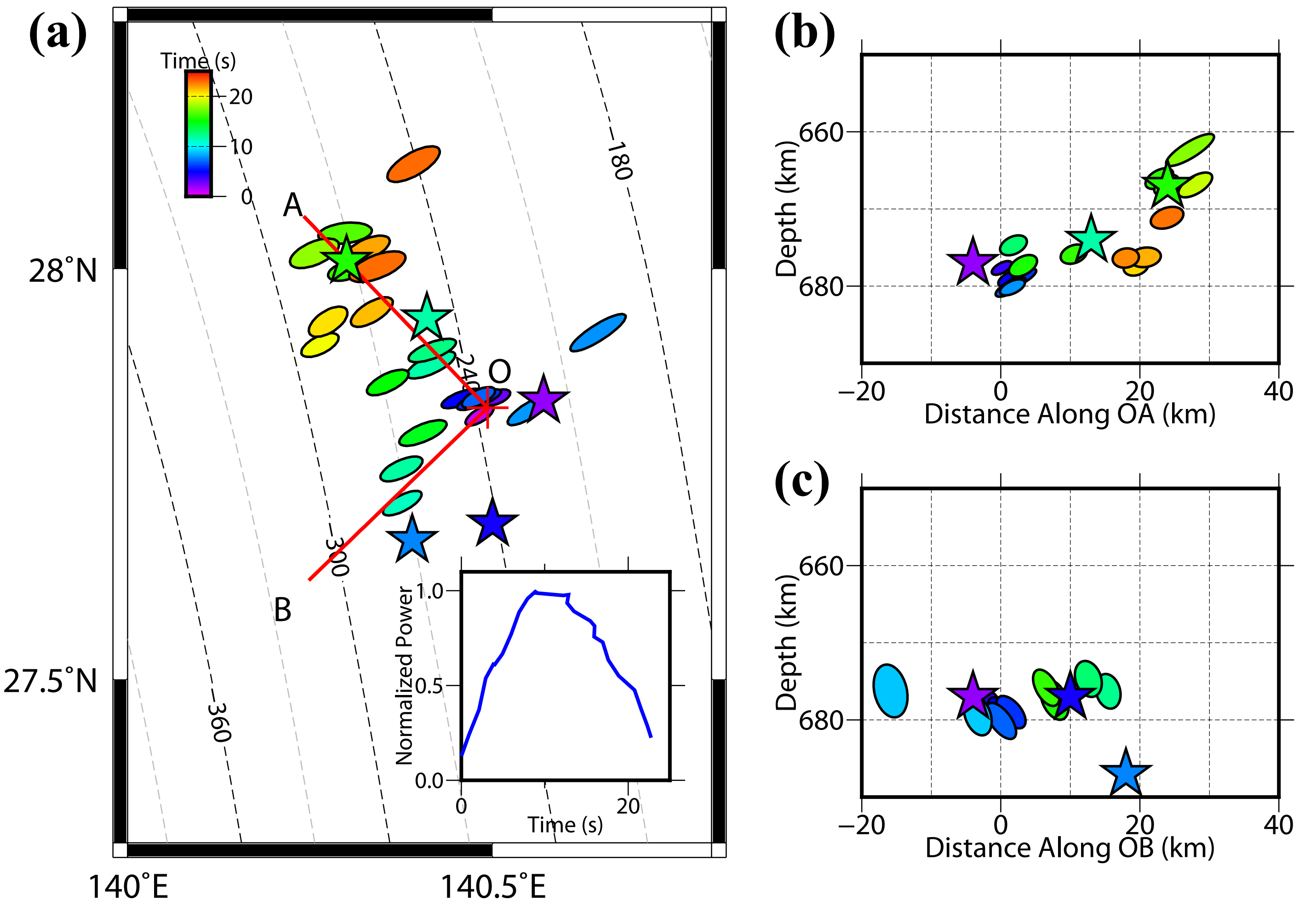
(a)
Time (s)
20
10
0
A
O
B
28˚N
27.5˚N
140˚E
140.5˚E
180
240
300
360
Normalized Power
1.0
0.5
0.0
0
20
Time (s)
(b)
Depth (km)
660
680
−20
0
20
40
Distance Along OA (km)
(c)
Depth (km)
660
680
−20
0
20
40
Distance Along OB (km)

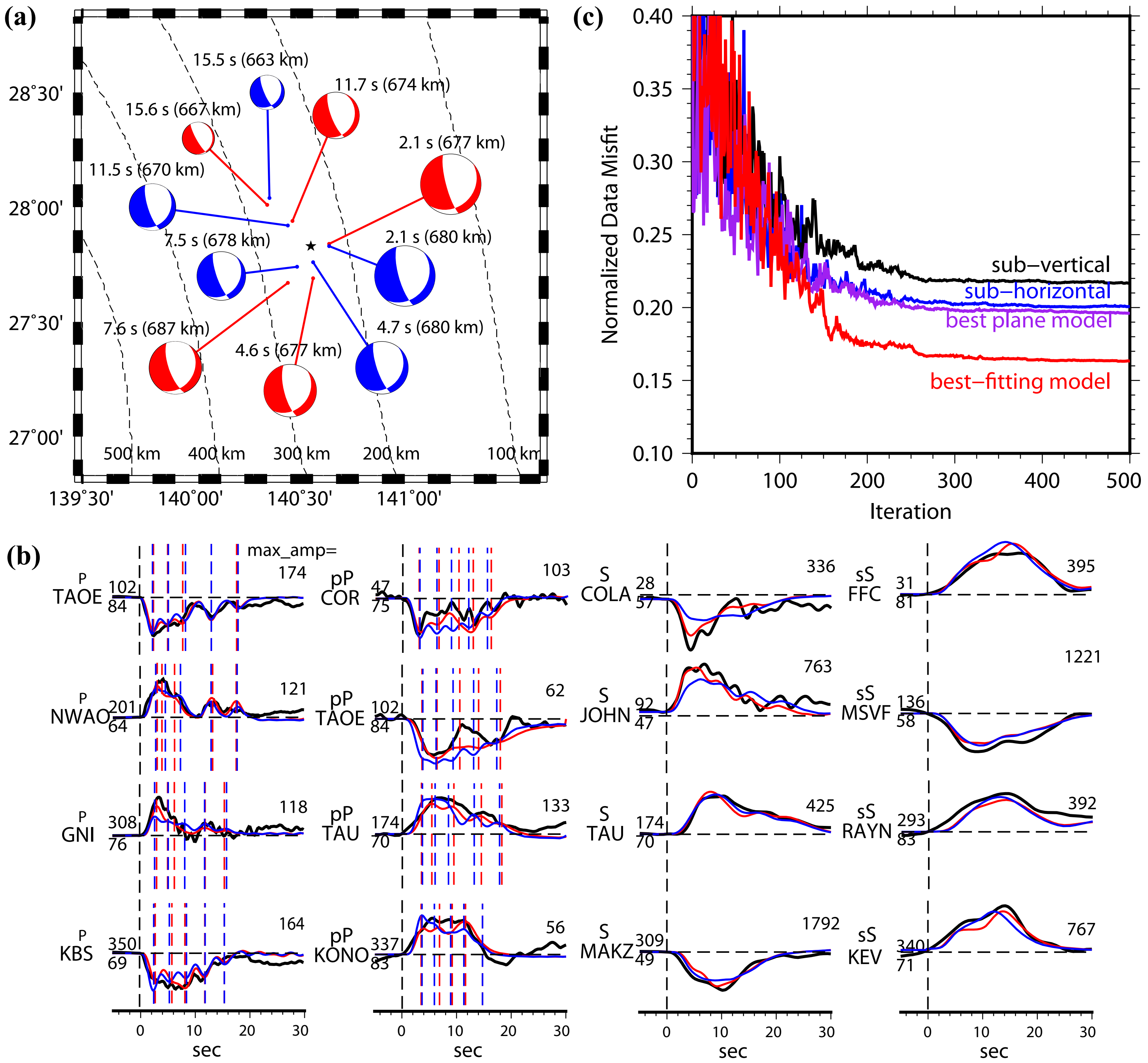

(a)
15.5 s (663 km)
11.7 s (674 km)
15.6 s (667 km)
2.1 s (677 km)
11.5 s (670 km)
7.5 s (678 km)
2.1 s (680 km)
7.6 s (687 km)
4.7 s (680 km)
4.6 s (677 km)
28°30'
28°00'
27°30'
27°00'
500 km
400 km
300 km
200 km
100 km
139°30'
140°00'
140°30'
141°00'
(c)
Normalized Data Misfit
Iteration
sub−vertical
sub−horizontal
best plane model
best−fitting model
(b)
max_amp=
P TAOE
P NWAO
P GNI
P KBS
pP COR
pP TAOE
pP TAU
pP KONO
S COLA
S JOHN
S TAU
S MAKZ
sS FFC
sS MSVF
sS RAYN
sS KEV
sec

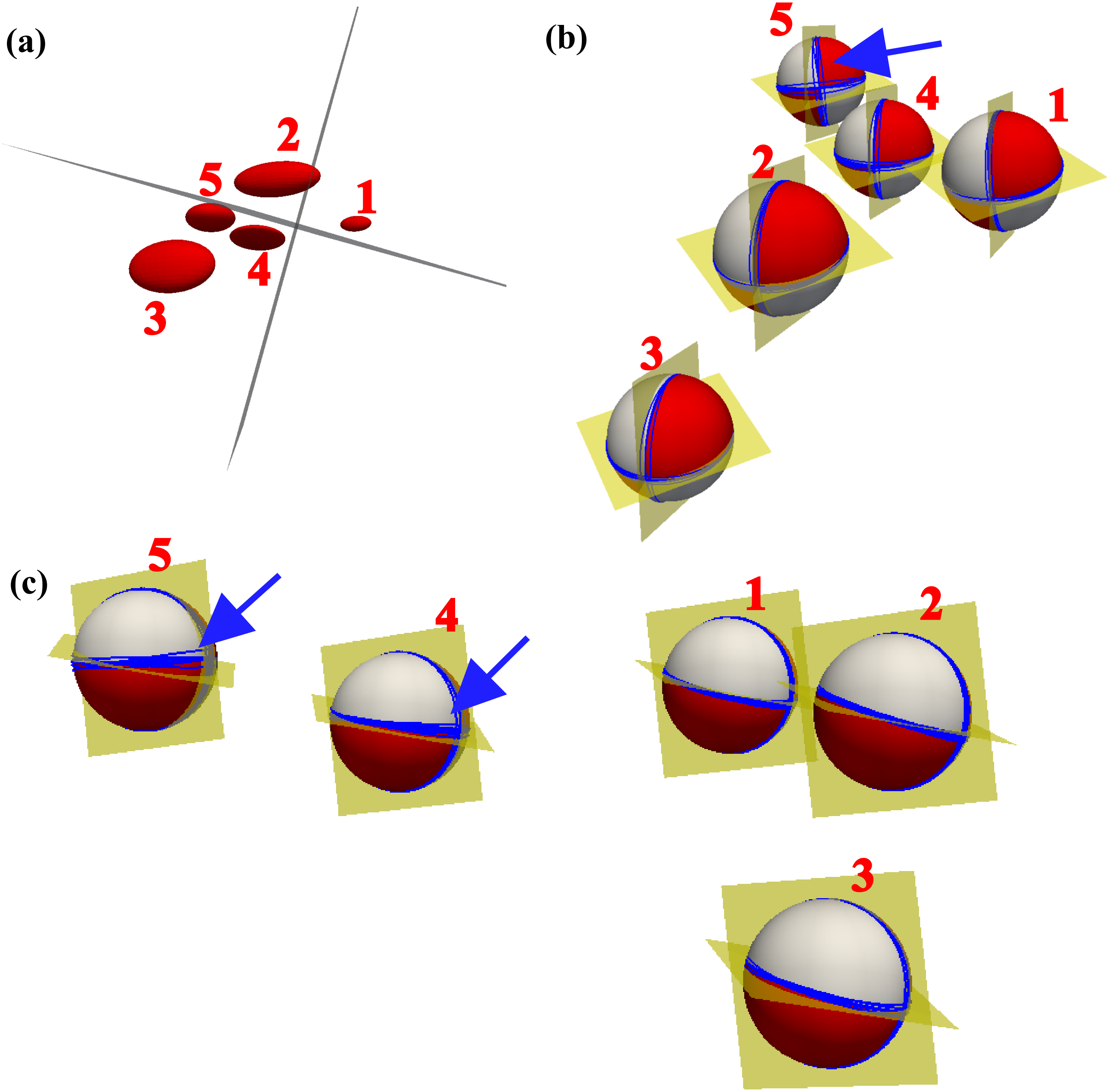
(a)
1
2
3
4
5
(b)
5
4
1
2
3
(c)
5
4
1
2
3

Geochemistry, Geophysics, Geosystems

Supporting Information for

Source complexity of the 2015 Mw 7.9 Bonin earthquake

Yu Chen[1,2,a,b], **Lingsen Meng**[3,a], **Ailin Zhang**[3], **Lianxing Wen**[1,4]

[1] Stony Brook University, Stony Brook, NY, 11794

[2] Los Alamos National Laboratory, Los Alamos, NM, 87545

[3] University of California, Los Angeles, CA, 90095

[4] Laboratory of Seismology and Physics of Earth's Interior; School of Earth and Space Sciences, University of Science and Technology of China, Hefei, Anhui, 230026

[a] Y.C. and L.M. equally contribute to this paper

[b] Corresponding author: Yu Chen (esschenyu@gmail.com)

Contents of this file

Figures S1 to S14

Tables S1 to S6

Introduction

The file contains Figures S1 – S14 and Tables S1 –S6 supplementary to the main text.

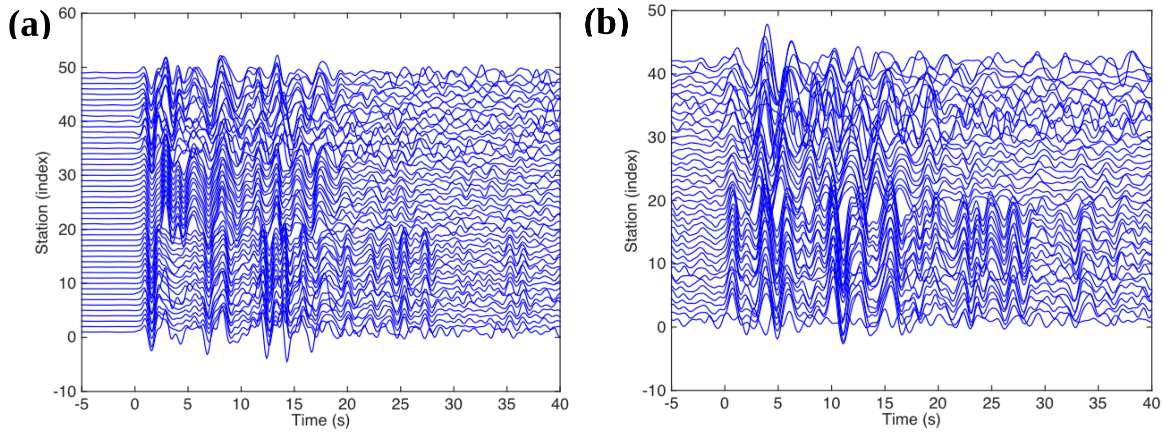

Figure S1. Mainshock (a) P- and (b) pP-waveforms recorded at Australian array filtered within 0.25~1 Hz. SNR for P: 43 dB, and SNR for pP: 15 dB.

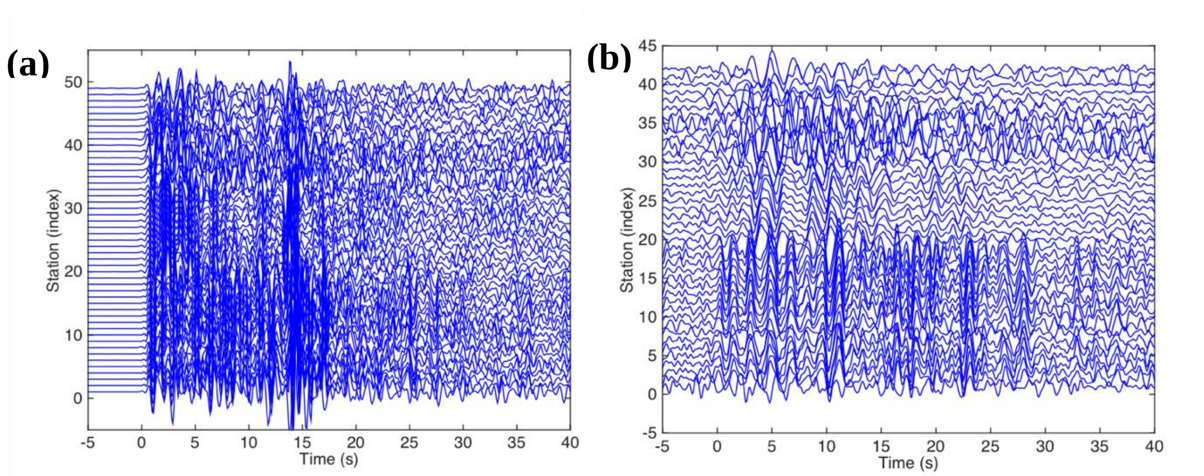

Figure S2. Mainshock (a) P- and (b) pP-waveforms recorded at Australian array filtered within 0.5~2 Hz. SNR for P:37 dB, and SNR for pP: 7 dB.

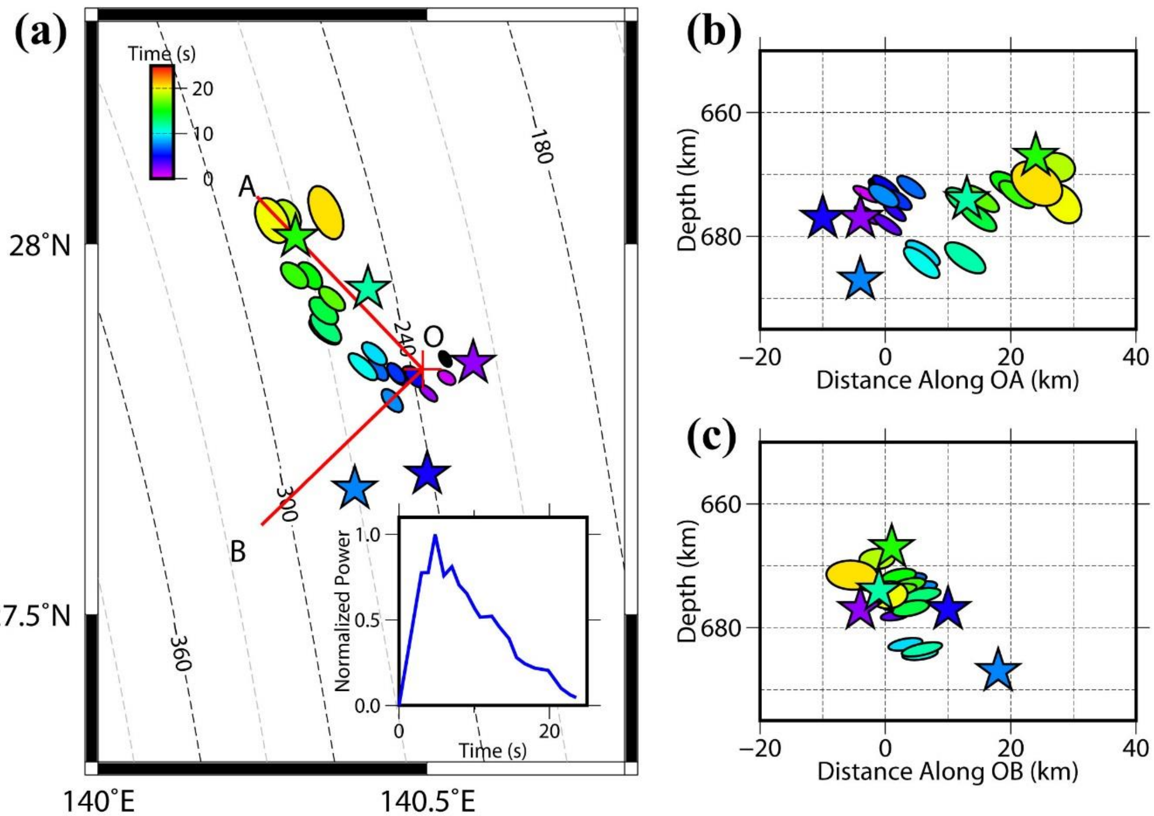

Figure S3. 3DBP image using the European (EU) network for the 2015 Mw 7.9 Bonin earthquake. (a) BP locations in map view. (b) Cross-section of BP images along OA in (a). (c) Cross-section of BP images along OB in (a). Inset map in (a) is normalized beamform power as a function of time. The colors and shapes of the ellipsoids demonstrate the timing and the 95% confidence interval on the peak locations. The colors and locations of the stars show the MSI inferred times and locations in Table S1.

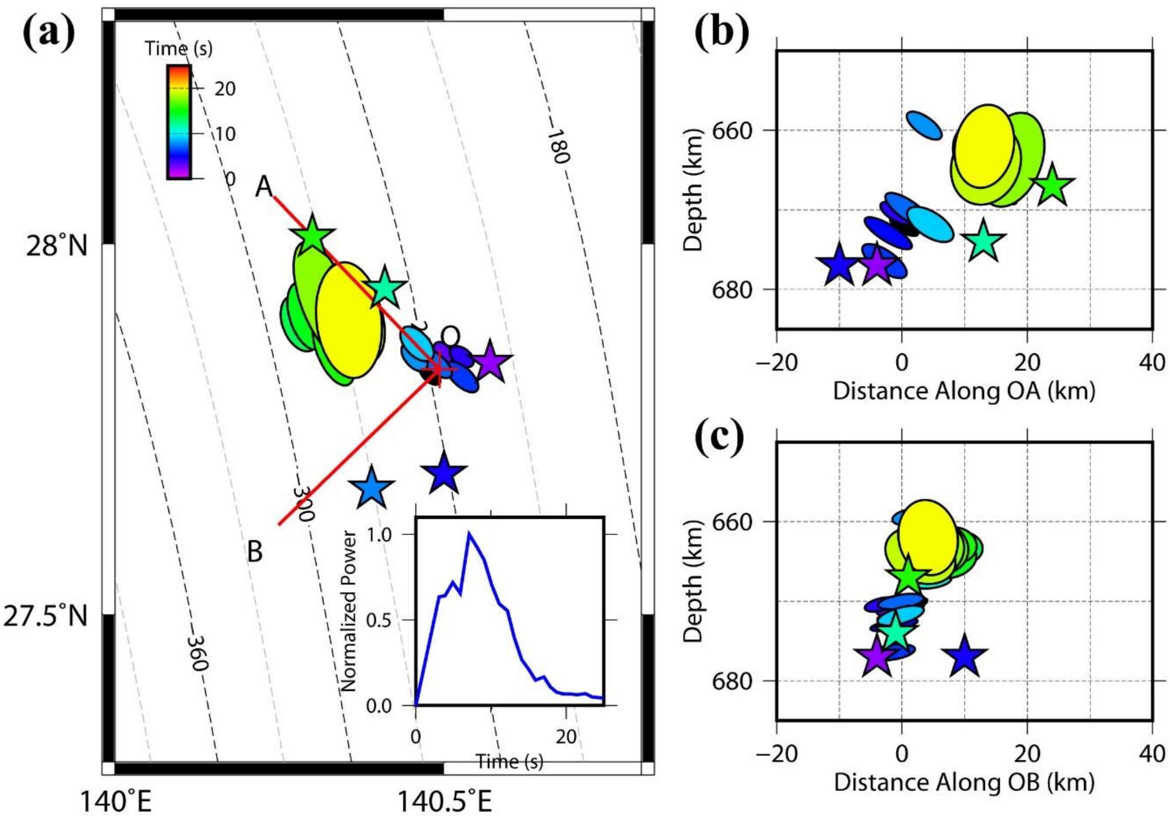

Figure S4. 3DBP image using the North American (NA) network for the 2015 Mw 7.9 Bonin earthquake. (a) BP locations in map view. (b) Cross-section of BP images along OA in (a). (c) Cross-section of BP images along OB in (a). Inset map in (a) is normalized beamform power as a function of time. The colors and shape of the ellipsoids demonstrate the timing and the 95% confidence interval on the peak locations. The colors and locations of the stars show the MSI inferred times and locations in Table S1.

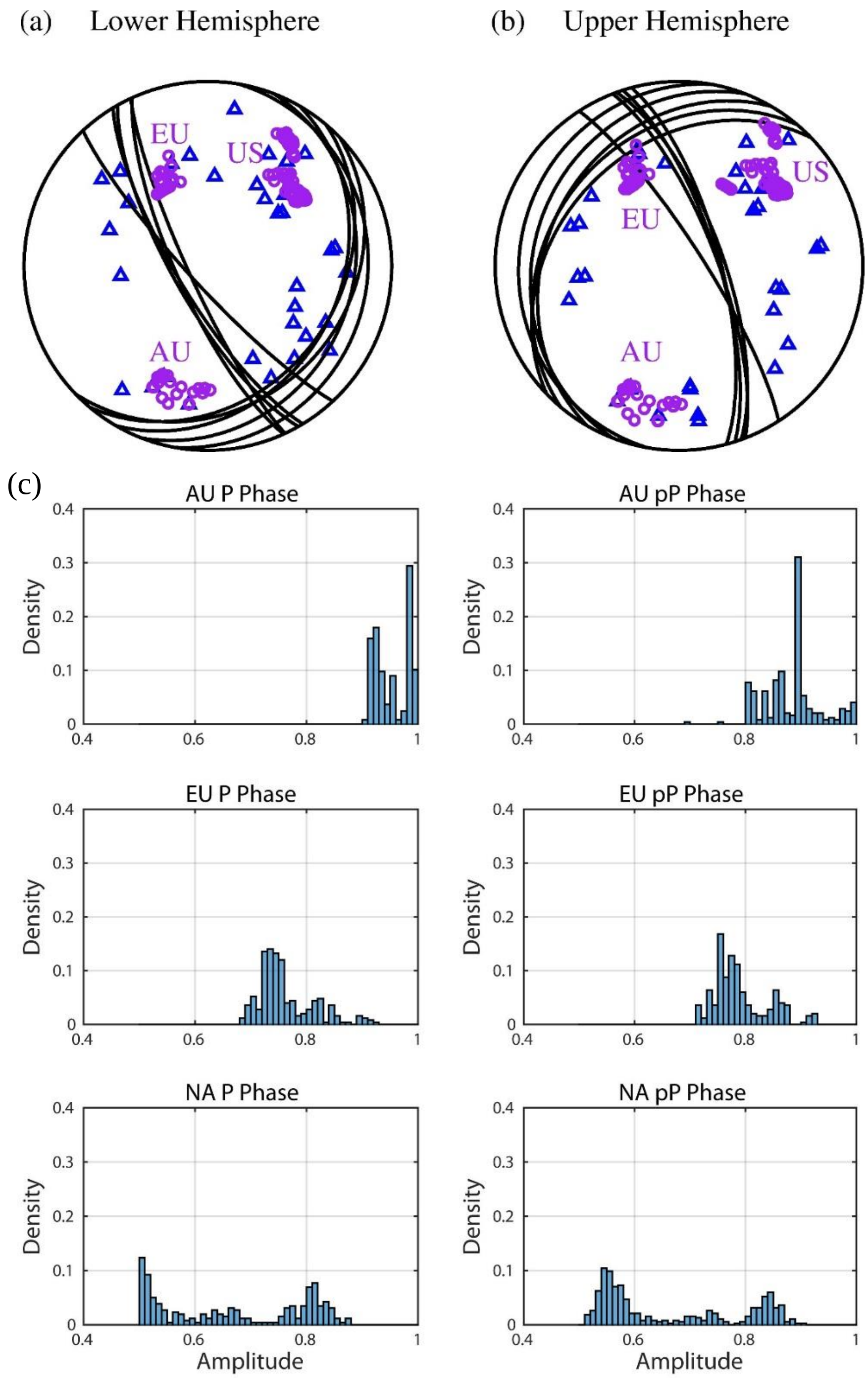

Figure S5. Take-off angles for the seismic rays from the AU, EU, and US arrays and the GSN stations shown on (a) upper hemisphere for P and SH waves and (b) lower hemisphere for pP and sSH waves. The purple circles represent take-off angles for (a) P and (b) pP waves for the stations of the three arrays, and the blue triangles are represents take-off angles for (a) P/SH and (b) pP/sSH waves for the GSN stations. (c) Density histogram of amplitudes of P and pP phases for all the networks.

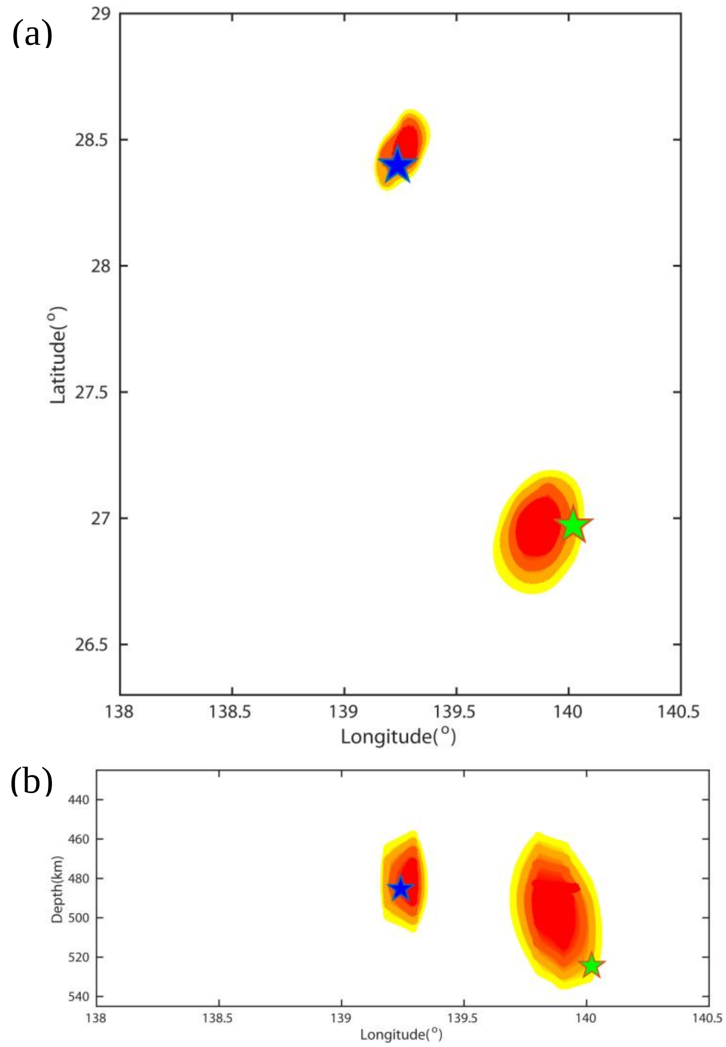

Figure S6. Resolution test of 3D back projection. Blue and green stars are ~M6 deep earthquakes occurred beneath Bonin Islands at 2010-11-30 and 2011-01-12 respectively. We back-projected the two events with a uniform timing correction acquired from cross-correlation of the blue star. This process is similar to imaging aftershocks with continuous data as described by Kiser and Ishii (2013). (a) denotes a horizontal map view of the 95% beam-forming power contour and hypocenter locations. (b) denotes a vertical cross section of the 95% beam-forming power contour and hypocenter locations.

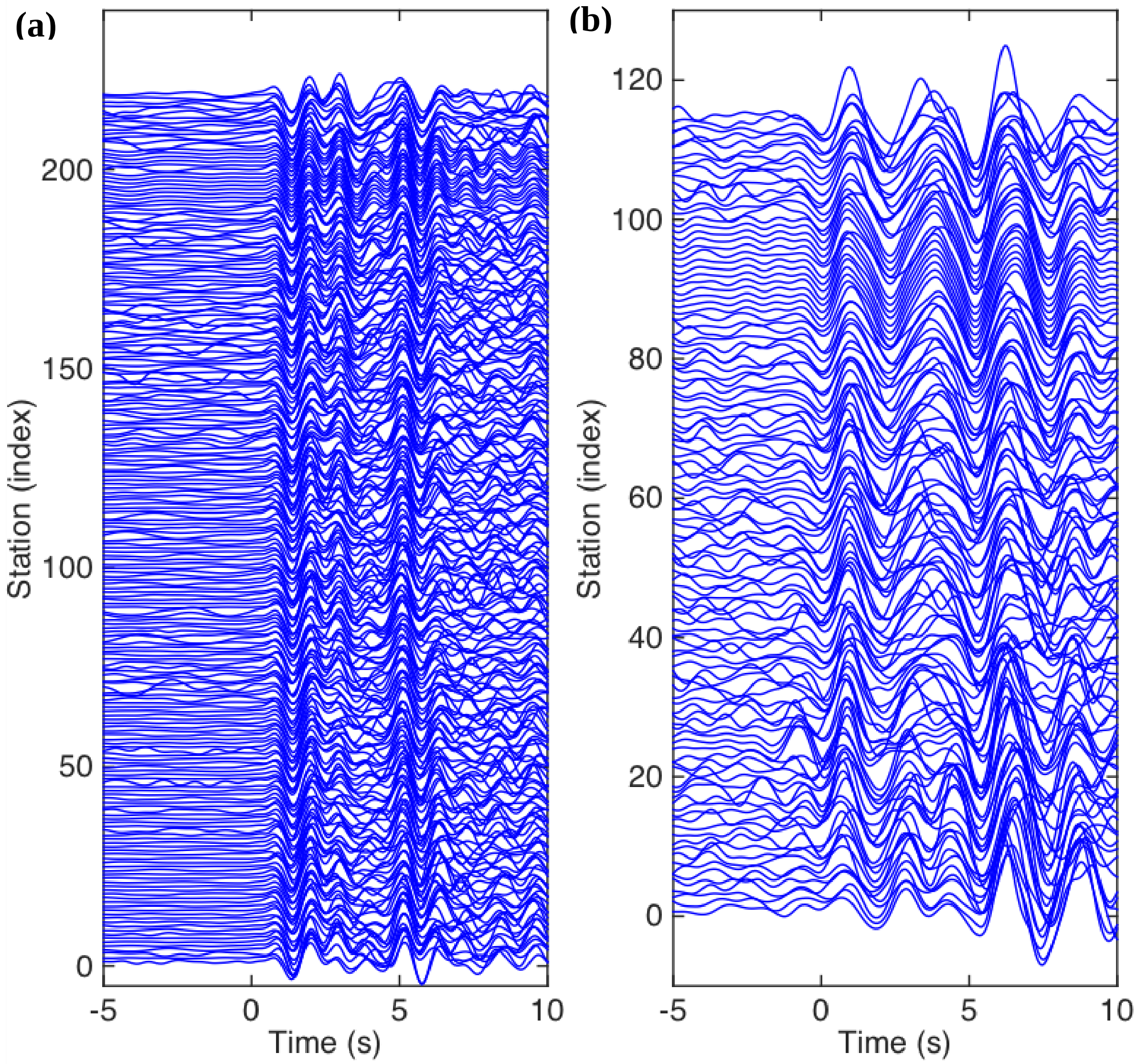

Figure S7. (a) P- and (b) pP-waveforms of empirical Green’s Function filtered within 0.25~1Hz. SNR for P: 20 dB, and SNR for pP: 12 dB.

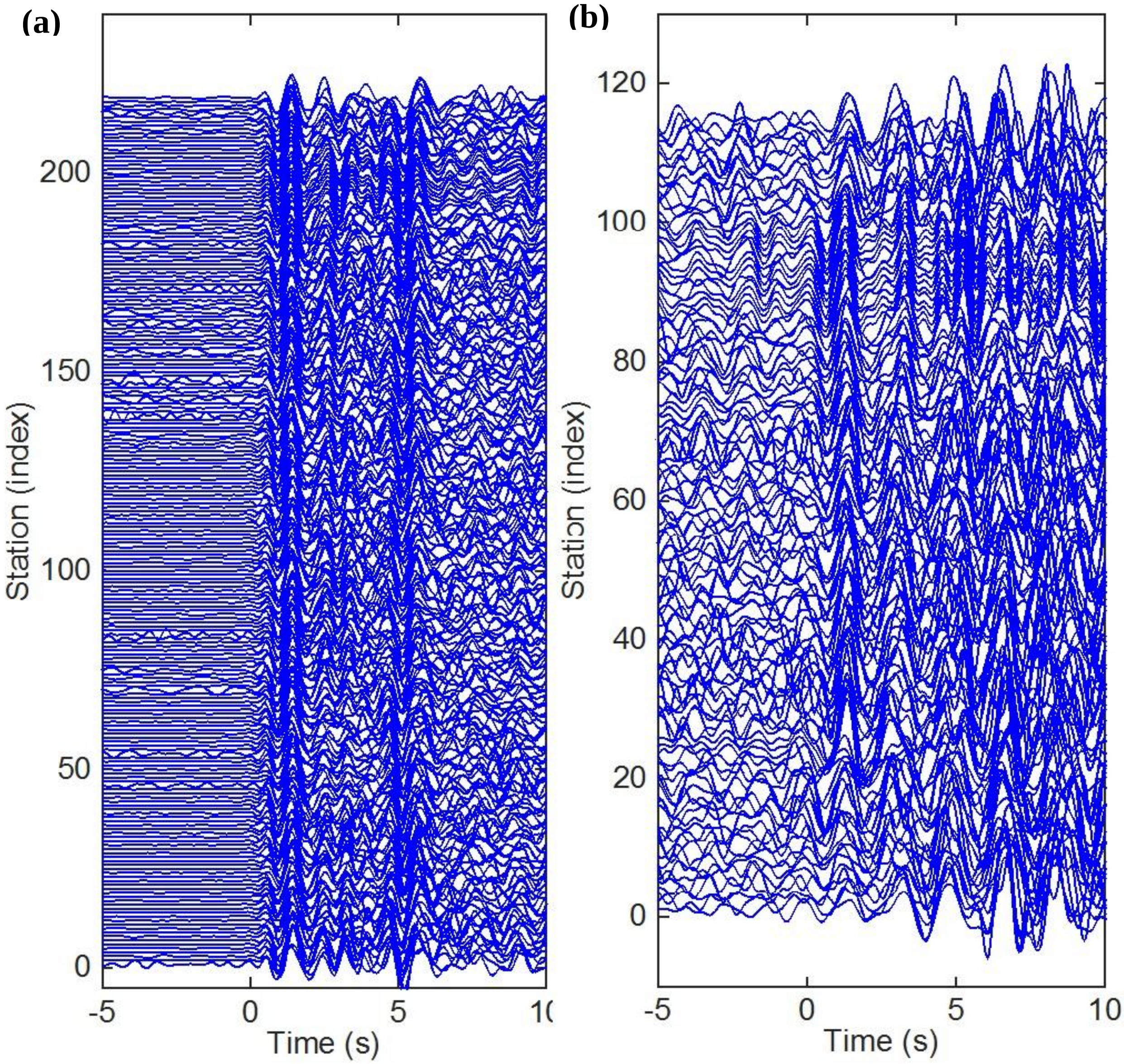

Figure S8. (a) P- and pP-waveforms of empirical Green's Function filtered within 0.5~2Hz. SNR for P: 31 dB, and SNR for pP: 11 dB.

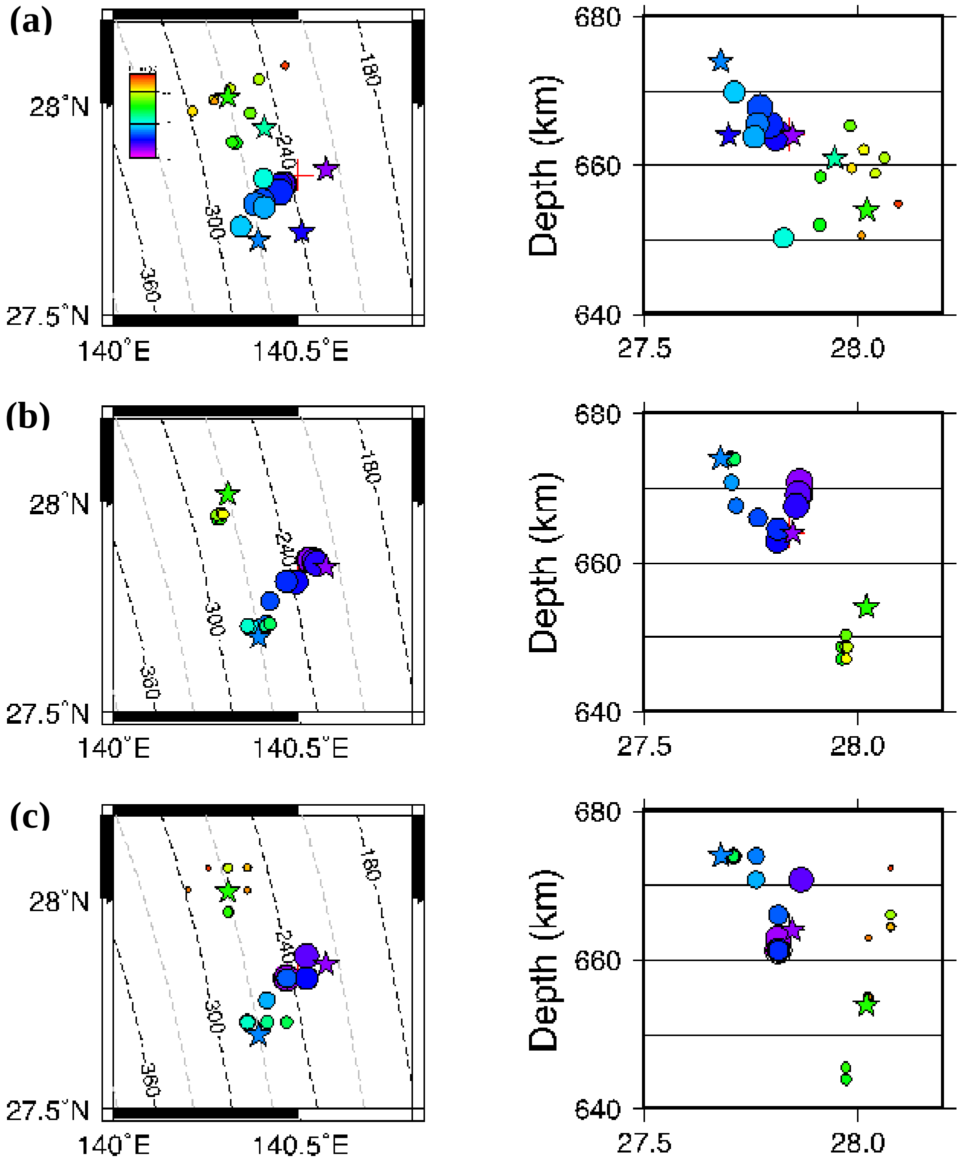

Figure S9. Synthetic test BP resolvability of continuous and discontinuous ruptures. (a) Continuous ruptures with 5 sources as listed in Table S1. Stars are input sources, cross is the hypocenter location and dots are BP radiators processed in 0.25 - 1 Hz. (Time scale is the same as Figures S3, S4) (b) Discontinuous ruptures with 3 separate sources (stars). The time separation is 5 s in the case and dots are resolved BP radiators in 0.25 – 1 Hz. (c) Same input setting as (b), but the BP is performed in 0.5 – 2 Hz.

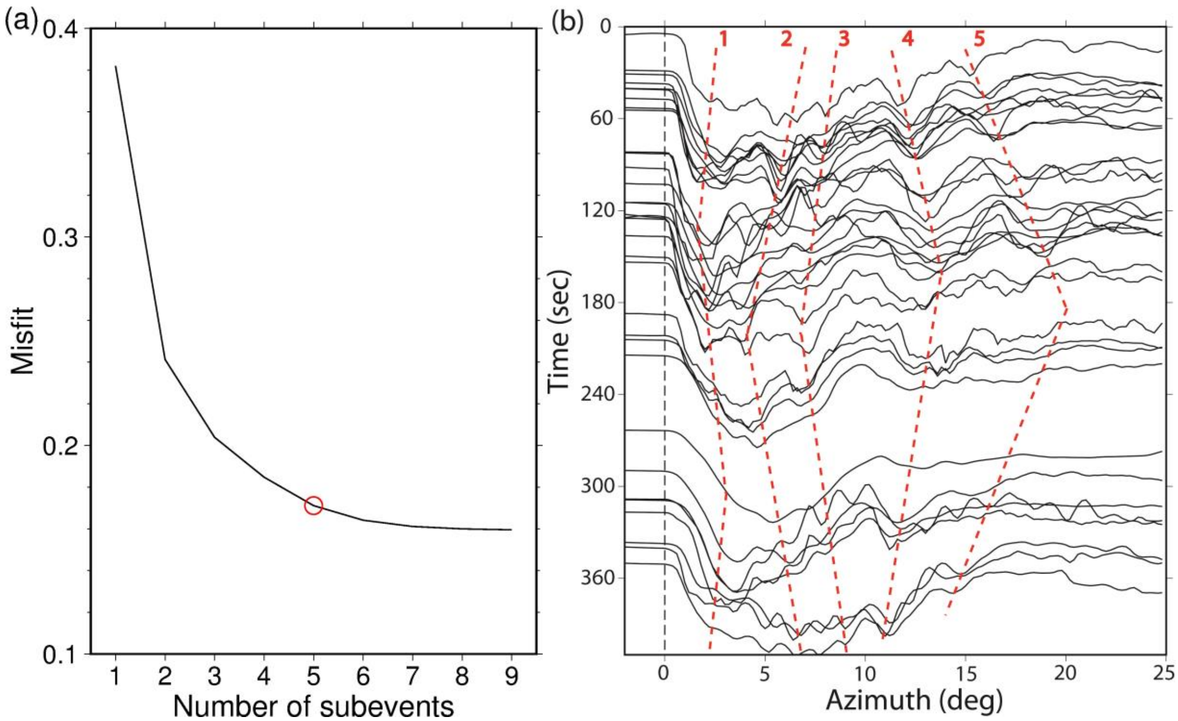

Figure S10. (a) The L-curve of normalized data misfit as a function of the sub-event number. (b) Observed vertical P displacement seismograms as a function of azimuths. Red dash lines highlight five coherent major energy pulses during the earthquake.

(a)

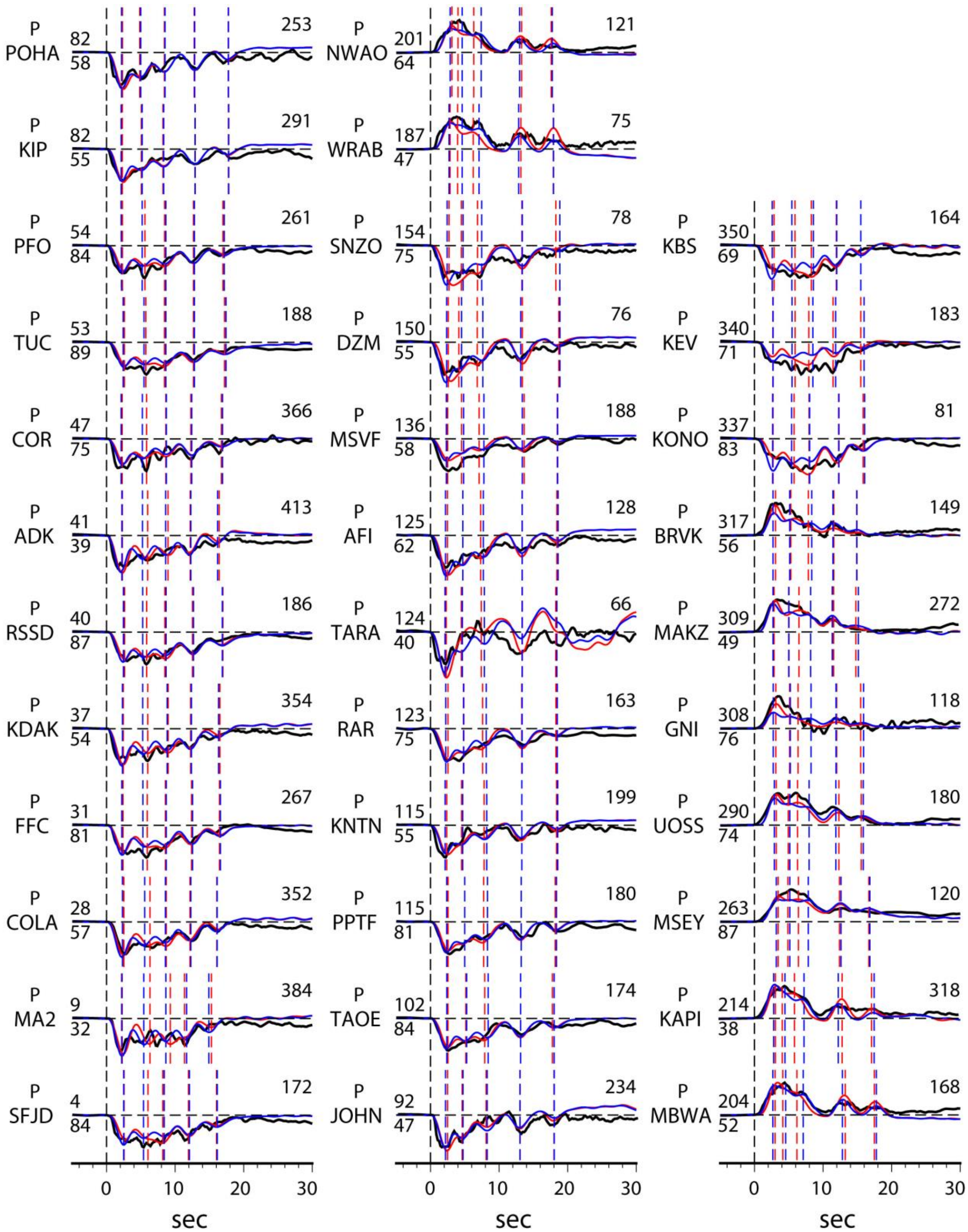
P POHA 82 58 253
P KIP 82 55 291
P PFO 54 84 261
P TUC 53 89 188
P COR 47 75 366
P ADK 41 39 413
P RSSD 40 87 186
P KDAK 37 54 354
P FFC 31 81 267
P COLA 28 57 352
P MA2 9 32 384
P SFJD 4 84 172
P NWAO 201 64 121
P WRAB 187 47 75
P SNZO 154 75 78
P DZM 150 55 76
P MSVF 136 58 188
P AFI 125 62 128
P TARA 124 40 66
P RAR 123 75 163
P KNTN 115 55 199
P PPTF 115 81 180
P TAOE 102 84 174
P JOHN 92 47 234
P KBS 350 69 164
P KEV 340 71 183
P KONO 337 83 81
P BRVK 317 56 149
P MAKZ 309 49 272
P GNI 308 76 118
P UOSS 290 74 180
P MSEY 263 87 120
P KAPI 214 38 318
P MBWA 204 52 168
0
10
20
30
sec

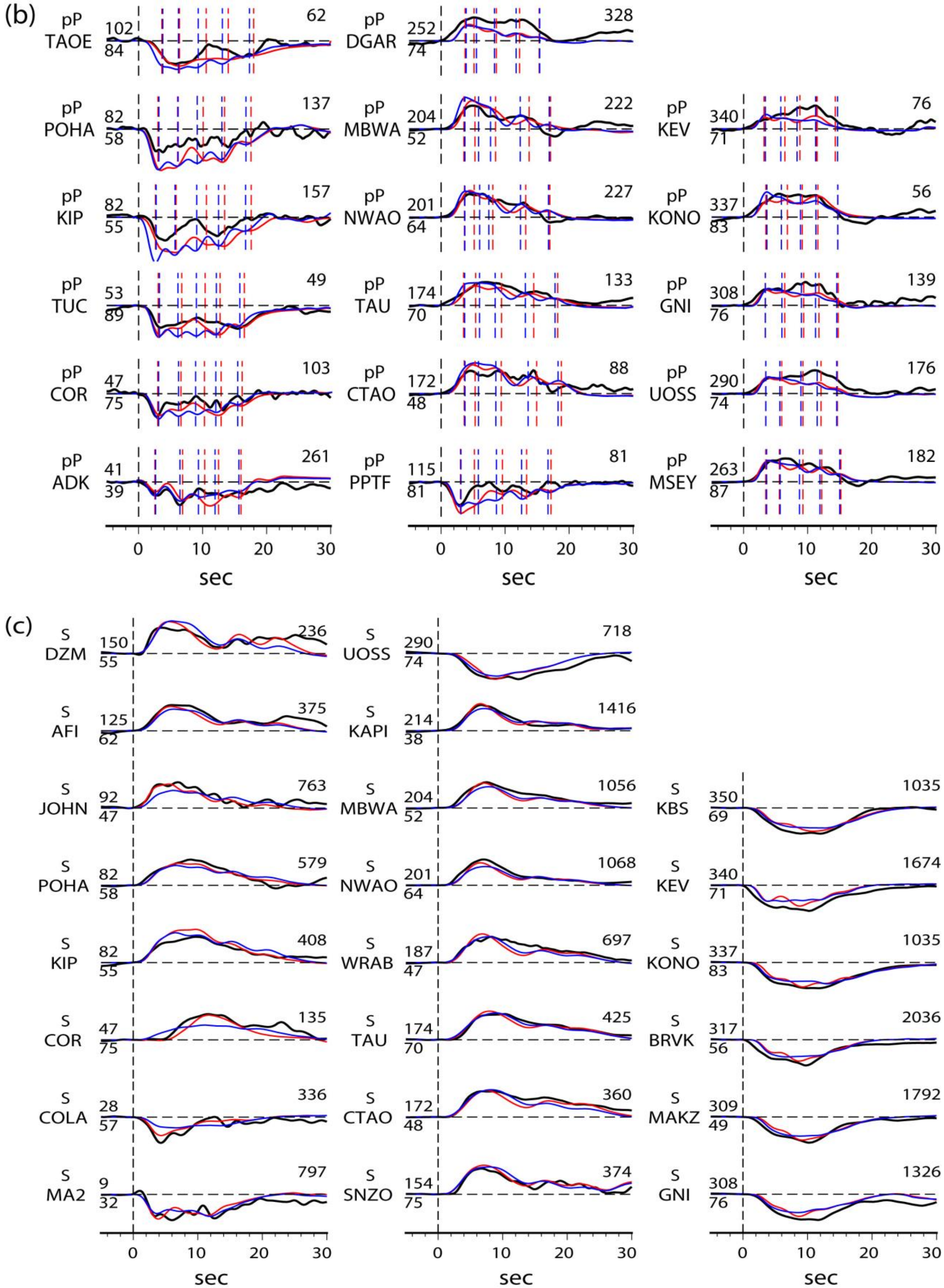
(b)
pP TAOE 102 84 62
pP DGAR 252 74 328
pP POHA 82 58 137
pP MBWA 204 52 222
pP KEV 340 71 76
pP KIP 82 55 157
pP NWAO 201 64 227
pP KONO 337 83 56
pP TUC 53 89 49
pP TAU 174 70 133
pP GNI 308 76 139
pP COR 47 75 103
pP CTAO 172 48 88
pP UOSS 290 74 176
pP ADK 41 39 261
pP PPTF 115 81 81
pP MSEY 263 87 182
0 10 20 30
sec
(c)
S DZM 150 55 236
S UOSS 290 74 718
S AFI 125 62 375
S KAPI 214 38 1416
S JOHN 92 47 763
S MBWA 204 52 1056
S KBS 350 69 1035
S POHA 82 58 579
S NWAO 201 64 1068
S KEV 340 71 1674
S KIP 82 55 408
S WRAB 187 47 697
S KONO 337 83 1035
S COR 47 75 135
S TAU 174 70 425
S BRVK 317 56 2036
S COLA 28 57 336
S CTAO 172 48 360
S MAKZ 309 49 1792
S MA2 9 32 797
S SNZO 154 75 374
S GNI 308 76 1326
0 10 20 30
sec

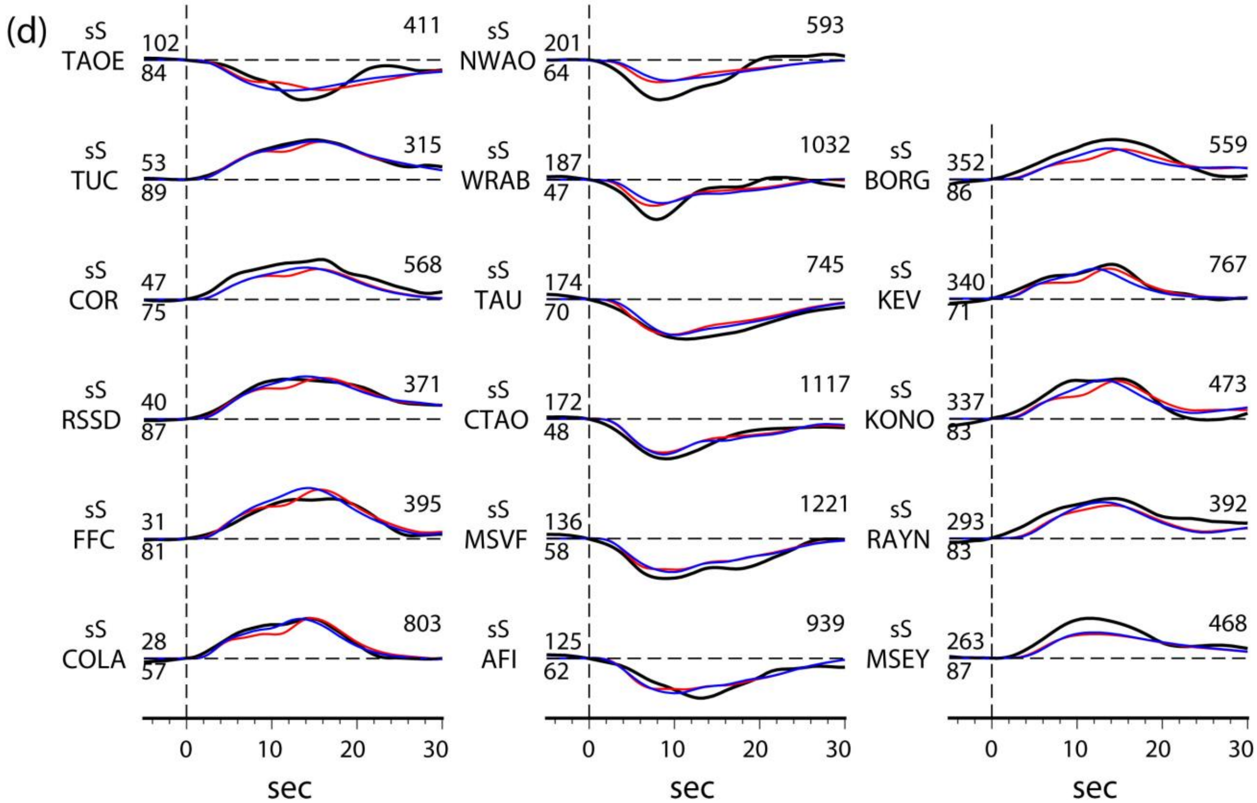

Figure S11. Observed seismograms (black traces) comparing with synthetics (red traces) predicted by the best-fitting sub-event model (Table S1) and synthetics (blue traces) predicted by the sub-event model with the sub-events compelled onto the GCMT sub-horizontal plane (Table S5), for (a) P waves, (b) pP waves, (c) SH waves and (d) sSH waves. The red and blue lines mark the peak times of the sub-events predicted by the best-fitting sub-event model and the sub-event model compelled onto the GCMT sub-horizontal, respectively. Seismic records are labeled with station name, phase, along with azimuth (up), epicentral distance (down), and the maximum amplitude of the data (right).

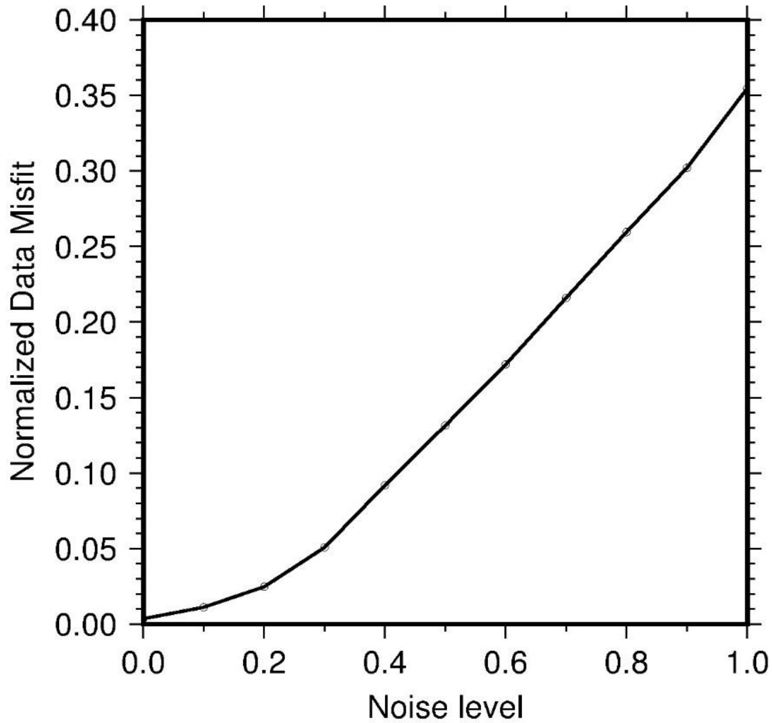

Figure S12. The normalized data misfits of the inversion result using the synthetic data with different noise level. We truncate the real noise before P wave arrival and normalize it to 0 – 100% of the maximum amplitude of the synthetic data.

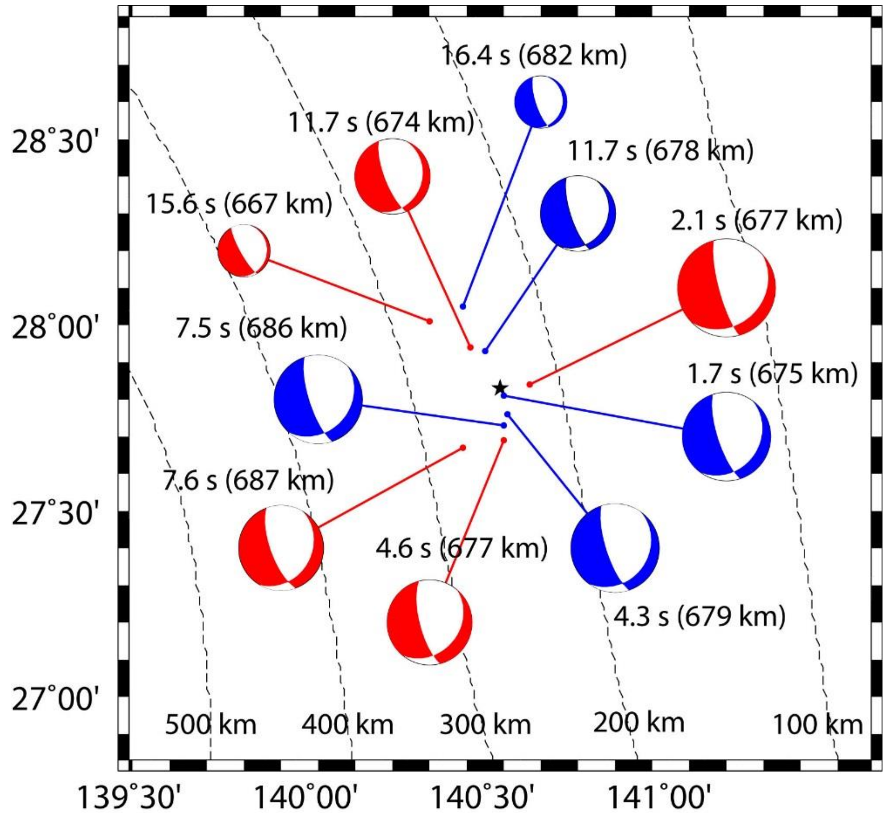

Figure S13. Locations of the best-fitting sub-event model (red points) and the sub-event model (blue points) compelled onto the GCMT sub-vertical plane, and the initiated location (black star), along with the slab depth contours (black traces, labeled with slab depths). Red and blue beach balls represent inferred focal mechanisms of the sub-events of the best-fitting sub-event model (Table S1) and the sub-event model compelled onto the GCMT sub-vertical plane (Table S6), labeled with the sub-event peak times, moment magnitudes and depths.

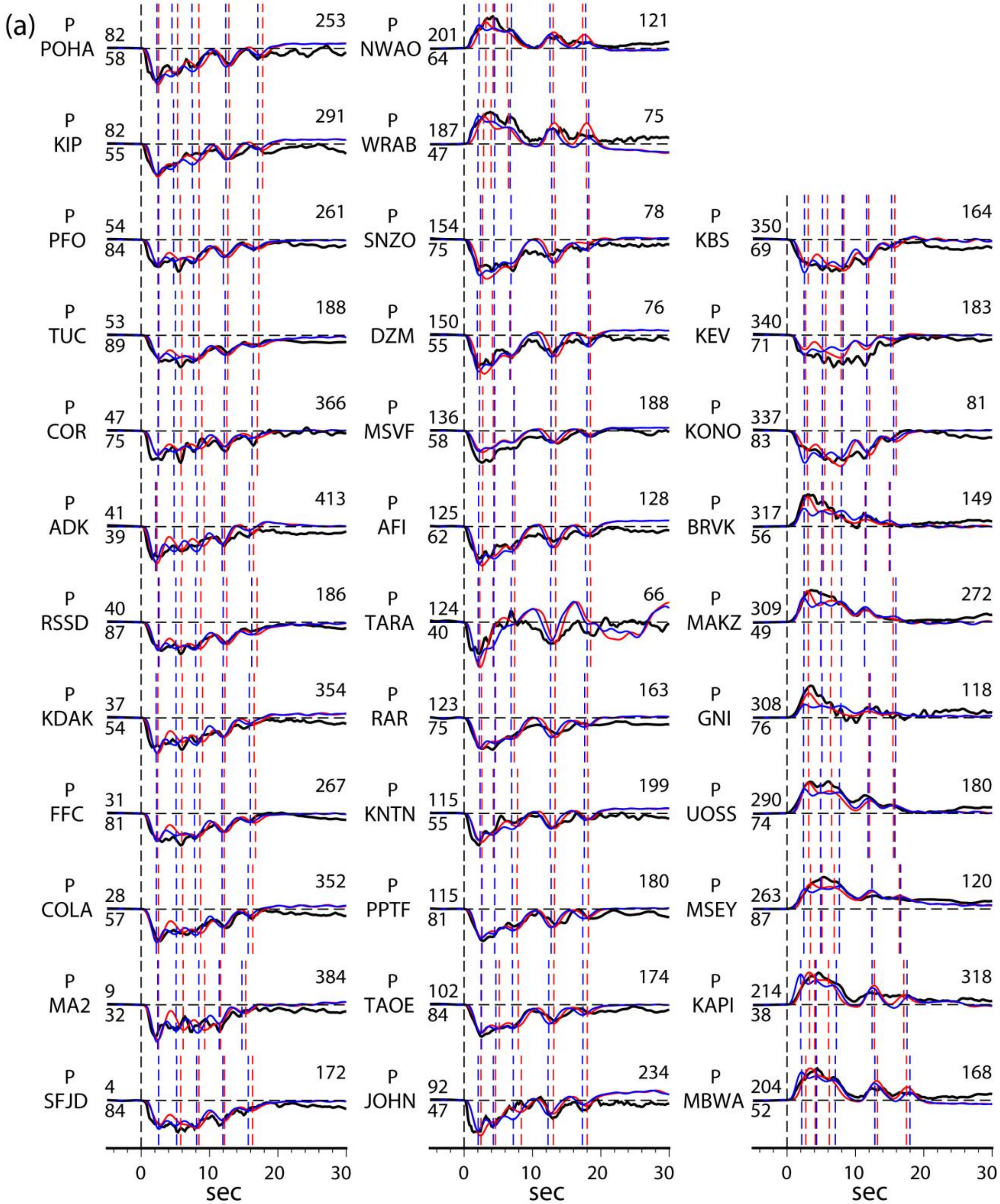
(a)
P POHA 82 58 253
P KIP 82 55 291
P PFO 54 84 261
P TUC 53 89 188
P COR 47 75 366
P ADK 41 39 413
P RSSD 40 87 186
P KDAK 37 54 354
P FFC 31 81 267
P COLA 28 57 352
P MA2 9 32 384
P SFJD 4 84 172
P NWAO 201 64 121
P WRAB 187 47 75
P SNZO 154 75 78
P DZM 150 55 76
P MSVF 136 58 188
P AFI 125 62 128
P TARA 124 40 66
P RAR 123 75 163
P KNTN 115 55 199
P PPTF 115 81 180
P TAOE 102 84 174
P JOHN 92 47 234
P KBS 350 69 164
P KEV 340 71 183
P KONO 337 83 81
P BRVK 317 56 149
P MAKZ 309 49 272
P GNI 308 76 118
P UOSS 290 74 180
P MSEY 263 87 120
P KAPI 214 38 318
P MBWA 204 52 168
0 10 20 30
sec

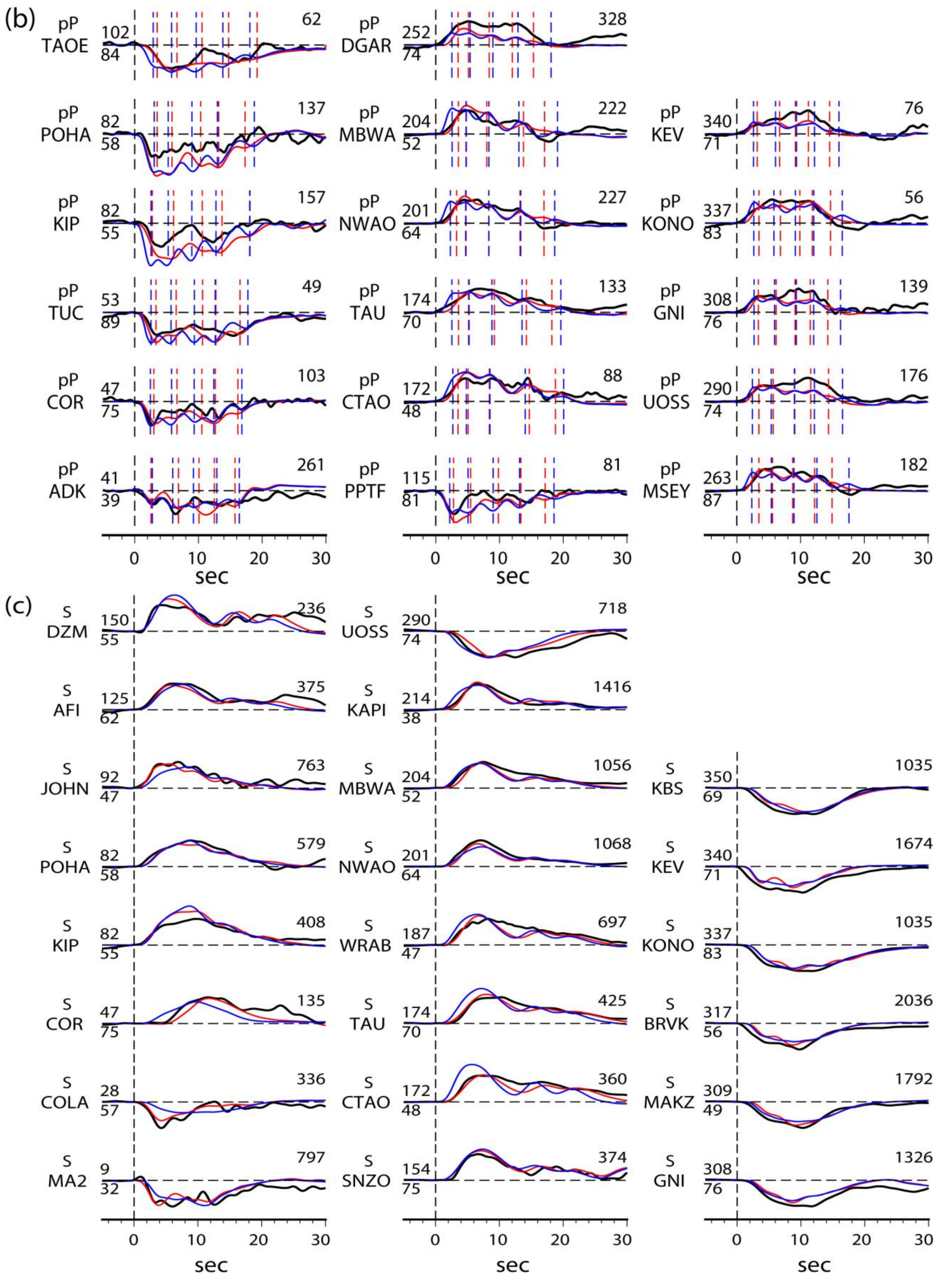
(b)
pP TAOE 102 84 62
pP DGAR 252 74 328
pP POHA 82 58 137
pP MBWA 204 52 222
pP KEV 340 71 76
pP KIP 82 55 157
pP NWAO 201 64 227
pP KONO 337 83 56
pP TUC 53 89 49
pP TAU 174 70 133
pP GNI 308 76 139
pP COR 47 75 103
pP CTAO 172 48 88
pP UOSS 290 74 176
pP ADK 41 39 261
pP PPTF 115 81 81
pP MSEY 263 87 182
0 10 20 30
sec
(c)
S DZM 150 55 236
S UOSS 290 74 718
S AFI 125 62 375
S KAPI 214 38 1416
S JOHN 92 47 763
S MBWA 204 52 1056
S KBS 350 69 1035
S POHA 82 58 579
S NWAO 201 64 1068
S KEV 340 71 1674
S KIP 82 55 408
S WRAB 187 47 697
S KONO 337 83 1035
S COR 47 75 135
S TAU 174 70 425
S BRVK 317 56 2036
S COLA 28 57 336
S CTAO 172 48 360
S MAKZ 309 49 1792
S MA2 9 32 797
S SNZO 154 75 374
S GNI 308 76 1326
0 10 20 30
sec

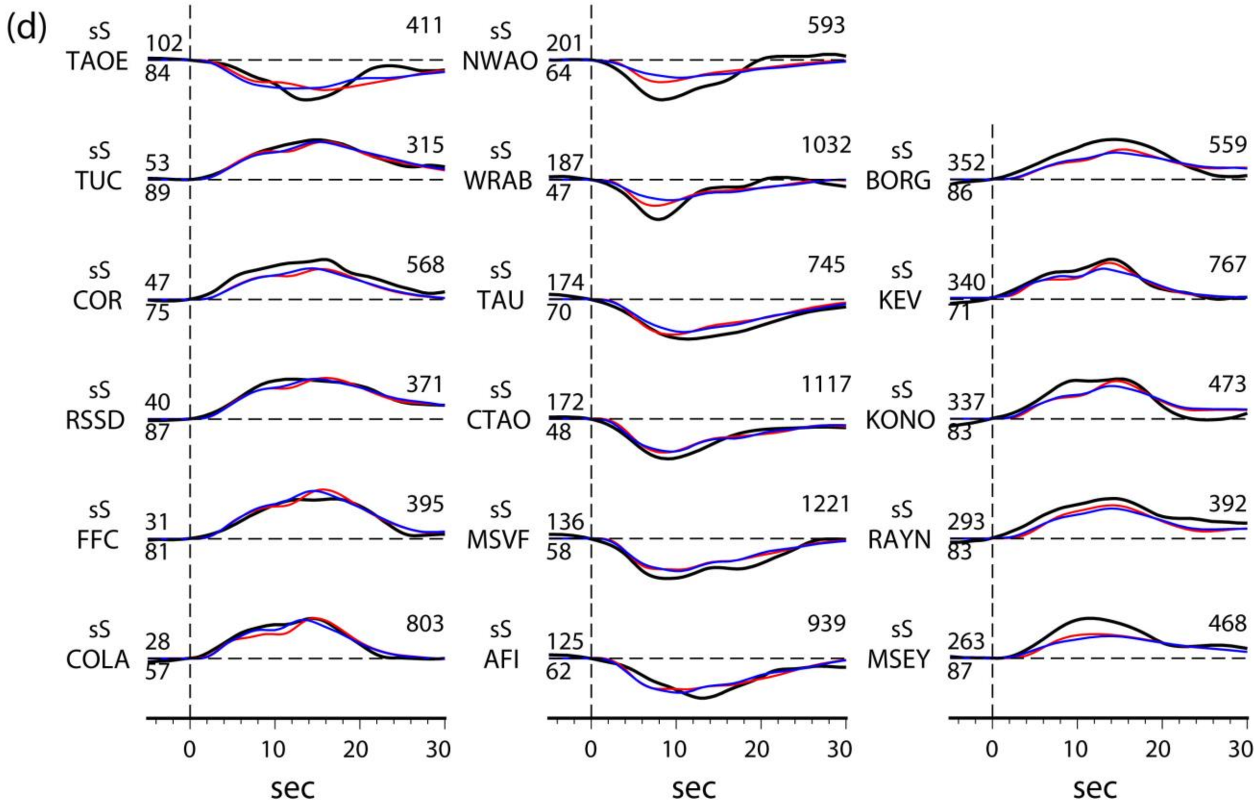

Figure S14. Observed seismograms (black traces) comparing with synthetics (red traces) predicted by the best-fitting sub-event model (Table S1) and synthetics (blue traces) predicted by the model with sub-events compelled onto the GCMT sub-vertical plane (Table S6), for (a) P waves, (b) pP waves, (c) SH waves and (d) sSH waves. The red and blue lines mark the peak times of the sub-events predicted by the best-fitting sub-event model and the sub-event model compelled onto the GCMT sub-vertical plane, respectively. Seismic records are labeled with station name, phase, along with azimuth (up), epicentral distance (down), and the maximum amplitude of the data (right).

Table S1. Source parameters of the best-fitting five sub-events of the Bonin Earthquake inferred by multiple-source inversion, dt presents occurring time, dn, de, and dz represent event location in north, east and vertical direction, duration represents seismic duration, strike, dip and slip represent strike, dip and slip angles for focal mechanism.

Sub-event	dt (s)	dn (km)	de (km)	dz (km)	duration (s)	moment (N-m)	strike (°)	dip (°)	slip (°)
1	2.1	0.7	7.7	0.0	3.6	2.0E+20	46.5	25.1	329.1
2	4.6	-16.0	1.3	0.0	3.8	1.4E+20	40.0	30.3	320.5
3	7.6	-18.0	-10.1	10.0	4.4	1.7E+20	30.1	29.3	316.1
4	11.7	11.7	-8.2	-3.0	4.0	1.4E+20	21.2	22.3	310.2
5	15.6	20.0	-18.2	-10.0	4.0	6.0E+19	10.0	13.8	312.0

Table S2. Source parameter uncertainties for noise-free synthetic data generated by the best-fitting five sub-event model (Table 1)

Sub-event	dt (s)	dn (km)	de (km)	dz (km)	duration (s)	moment (%)	strike (°)	dip (°)	slip (°)
1	0.08	1	1	1	0.15	2	3	1	3
2	0.13	2	2	2	0.42	6	3	2	3
3	0.17	2	3	2	0.41	6	3	1	3
4	0.11	2	2	2	0.36	6	4	1	3
5	0.20	3	3	3	0.30	4	5	2	5

Table S3. Source parameter uncertainties for synthetic data generated by the best-fitting five sub-event model (Table 1), with the real seismic noise normalized to 80% of the maximum amplitudes of the seismic data

Sub-event	dt (s)	dn (km)	de (km)	dz (km)	duration (s)	moment (%)	strike (°)	dip (°)	slip (°)
1	0.14	2	3	3	0.18	6	3	2	4
2	0.21	3	3	3	0.50	9	7	2	7
3	0.30	4	3	3	0.44	7	4	2	4
4	0.25	4	3	3	0.46	9	5	2	5
5	0.32	4	4	3	0.48	8	8	5	9

Table S4. Source parameter uncertainties for the bootstrap inversion that randomly select 80% of the waveforms using in our inversion (Table S1)

Sub-event	dt (s)	dn (km)	de (km)	dz (km)	duration (s)	moment (%)	strike (°)	dip (°)	slip (°)
1	0.04	2	1	1	0.14	7	3	2	3
2	0.20	5	2	2	0.42	15	4	2	3
3	0.19	5	2	3	0.26	9	5	1	4
4	0.52	4	5	1	0.39	6	7	2	6
5	0.45	4	4	2	0.45	8	8	4	7

Table S5. Source parameters of the sub-event model with the five sub-events compelled onto the GCMT sub-horizontal plane

Sub-event	dt (s)	dn (km)	de (km)	dz (km)	duration (s)	moment (N-m)	strike (°)	dip (°)	slip (°)
1	2.1	0.0	7.8	3.0	3.1	2.0E+20	37.0	26.0	320.0
2	4.7	-7.4	0.5	2.4	4.4	1.6E+20	37.0	26.0	323.0
3	7.5	-10.4	-6.1	0.7	4.4	1.4E+20	37.0	26.0	324.2
4	11.5	10.3	-9.8	-6.9	4.0	1.3E+20	37.0	26.0	322.1
5	15.5	24.1	-17.4	-13.9	4.0	7.0E+19	37.0	26.0	328.0

Table S6. Source parameters of the sub-event model with the five sub-events compelled onto the GCMT sub-vertical plane

Sub-event	dt (s)	dn (km)	de (km)	dz (km)	duration (s)	moment (N-m)	strike (°)	dip (°)	slip (°)
1	1.7	-2.5	1.3	-1.7	2.5	1.7E+20	162.0	74.0	249.2
2	4.3	-7.8	2.0	1.8	4.4	1.7E+20	162.0	74.0	249.6
3	7.5	-10.6	0.7	8.9	4.4	1.7E+20	162.0	74.0	245.0
4	11.7	11.1	-3.7	0.4	4.0	1.3E+20	162.0	74.0	253.4
5	16.4	25.0	-9.6	5.1	4.0	6.0E+19	162.0	74.0	261.3